Medical image reconstruction with multi-level deep learning denoiser and tight frame regularization

Tingting Wu[a], Chaoyan Huang[d], Shilong Jia[b], Wei Li[a], Raymond Chan[c], Tieyong Zeng[d,*], S. Kevin Zhou[e,f]

[a]*School of Science, Nanjing University of Posts and Telecommunications, Nanjing, China*
[b]*School of Computer Science, Nanjing University of Posts and Telecommunications, Nanjing, China*
[c]*Department of Mathematics, City University of Hong Kong, Hong Kong*
[d]*Department of Mathematics, The Chinese University of Hong Kong, Shatin, Hong Kong*
[e]*MIRACLE group, Key Laboratory of Intelligent Information Processing of CAS, ICT, CAS, Beijing, 100190, China*
[f]*University of the Chinese Academy of Sciences (UCAS), Beijing, 100049, China*

Abstract

As a fundamental task, medical image reconstruction has attracted growing attention in clinical diagnosis. Aiming at promising performance, it is critical to deeply understand and effectively design advanced model for image reconstruction. Indeed, one possible solution is to integrate the deep learning methods with the variational approaches to absorb benefits from both parts. In this paper, to protect more details and a better balance between the computational burden and the numerical performance, we carefully choose the multi-level wavelet convolutional neural network (MWCNN) for this issue. As the tight frame regularizer has the capability of maintaining edge information in image, we combine the MWCNN with the tight frame regularizer to reconstruct images. The proposed model can be solved by the celebrated proximal alternating minimization (PAM) algorithm. Furthermore, our method is a noise-adaptive framework as it can also handle real-world images. To prove the robustness of our strategy, we address two important medical image reconstruction tasks: Magnetic Resonance Imaging (MRI) and Positron Emission Tomography (PET). Extensive numerical experiments show clearly that our approach achieves better performance over several state-of-the-art methods.

Keywords: Medical image reconstruction, Multi-level wavelet convolutional neural network, Tight frame, Proximal alternating minimization, Magnetic resonance imaging, Positron emission tomography

1. Introduction

Image reconstruction aims to build two-dimensional or three-dimensional images based on incomplete data. This is an essential task in medical imaging as the reconstructed results will seriously affect the diagnosis results. During the past decades, many excellent methods have been applied for medical image reconstruction [1, 2, 3]. Assuming that f is the observation, the general image reconstruction task can be formulated as the following minimization problem

$$\min_u \Phi(Au, f) + \eta R(u), \tag{1}$$

where A is a known linear operator, u is the clear image to be sought, $\Phi(Au, f)$ is the data fidelity term, η is a positive parameter for balancing, and $R(u)$ is the regularization term. The data fidelity term of model (1) can be obtained by

---

*Corresponding author: zeng@math.cuhk.edu.hk.

applying the maximum a posteriori probability (MAP) estimation and Bayes rule [4]. In medical imaging, $\Phi(A_1u, f) = \|A_1u - f\|_2^2$ represents the Magnetic Resonance Imaging (MRI) image reconstruction task [5]. When it comes to Positron Emission Tomography (PET) image reconstruction task [6], $\Phi(A_2u, f) = \langle 1, A_2u + c \rangle - \langle f, \ln(A_2u + c) \rangle$. Here c is a constant, 1 is a matrix with all elements as 1 and has the same dimension of $A_2u + c$, A_1 and A_2 are the acquisition process operators of the PET and MRI, respectively, and $\langle \cdot \rangle$ is the inner product.

There are many significant regularizers for medical image reconstruction, which can generally be divided into traditional methods and deep learning-based schemes. Previously, several important handcrafted mathematical models have been carefully designed for image processing [7, 8, 9]. For example, the celebrated total variation (TV) regularizer [10, 11] was first proposed for gray image restoration and has shown success in medical image reconstruction [12]. Another notable regularizer is the wavelet framelet term [13], which can sparsely approximate piecewise smooth functions. Compared to other variational-based methods, the tight frame method has been proved to have better performance for fine structure [14]. There are also some researchers applying the tight frame in PET reconstruction to obtain competitive results [15]. Actually, the tight frame achieves outstanding performance in medical imaging. For instance, the authors in [16] proposed an adaptive tight frame for medical imaging. Later, Zhan and Dong [17] extended the tight frame to the spatial-radon domain, and this data-driven tight frame regularization generated good results in medical image reconstruction. However, most tight-frame-based approaches have drawbacks in having artifacts in image reconstruction tasks.

(a) IFFT (21.10/0.5678) (b) TV (23.96/0.6556) (c) DDTF (28.07/0.8036) (d) IRCNN (28.55/0.7956) (e) Ours (31.00/0.8461)

(a) EM (27.61/0.8251) (b) TV (31.08/0.9252) (c) DDTF (32.78/0.9345) (d) IRCNN (32.69/0.9242) (e) Ours (33.34/0.9404)
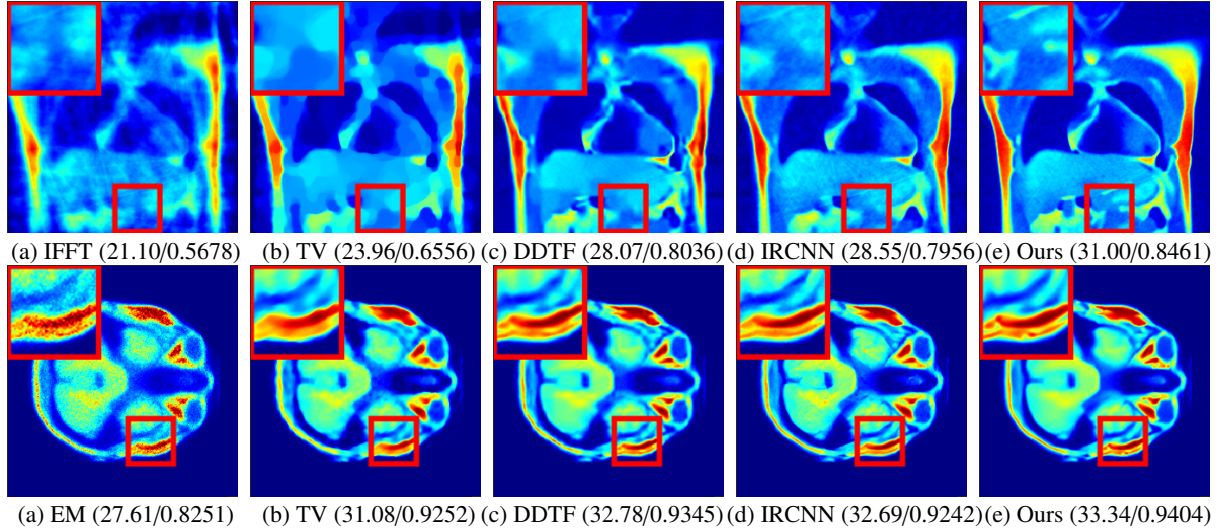
Figure 1. Reconstruction results (PSNR/SSIM). The first row is the MRI reconstruction results of image 'M12', the second row is the PET reconstruction results of image 'P05'. (a) IFFT and EM [18]; (b) TV [6]; (c) DDTF [15]; (d) IRCNN [19]; (e) Ours.

Recently, deep learning-based methods have shown great superiority in image processing [20, 21, 22]. For example, Li et al. [23] proposed a multiple degradation and reconstruction network for image denoising. Zhang et al. [19] proposed a deep convolutional neural network (CNN) denoiser model for image processing. Later, a novel deep denoiser named multi-level wavelet convolutional neural network (MWCNN) was investigated in [24], which achieves great success in image restoration with additive Gaussian noise. Later, Wu et al. [25] applied the MWCNN denoiser for Cauchy noise removal. Note that the MWCNN is good at preserving texture details. However, the interpretation of the deep learning-based schemes is still an open question [26]. Most deep learning-based methods are often regarded as black boxes, lacking transparency in their decision-making processes, particularly in attaining clear image outputs [27]. In the realm of medical imaging, these deep learning approaches encounter numerous challenges. Conversely, traditional methods fall short of efficiently accomplishing image reconstruction tasks. Consequently, our objective is to bridge this gap by synergistically employing traditional regularization techniques alongside deep learning methodologies for establishing an interpretable framework for image reconstruction. To realize this objective, we propose an integration of tight frame and MWCNN denoiser for medical image reconstruction. This approach effectively harnesses the strengths of both methodologies. Primarily, the proposed method showcases promising re-
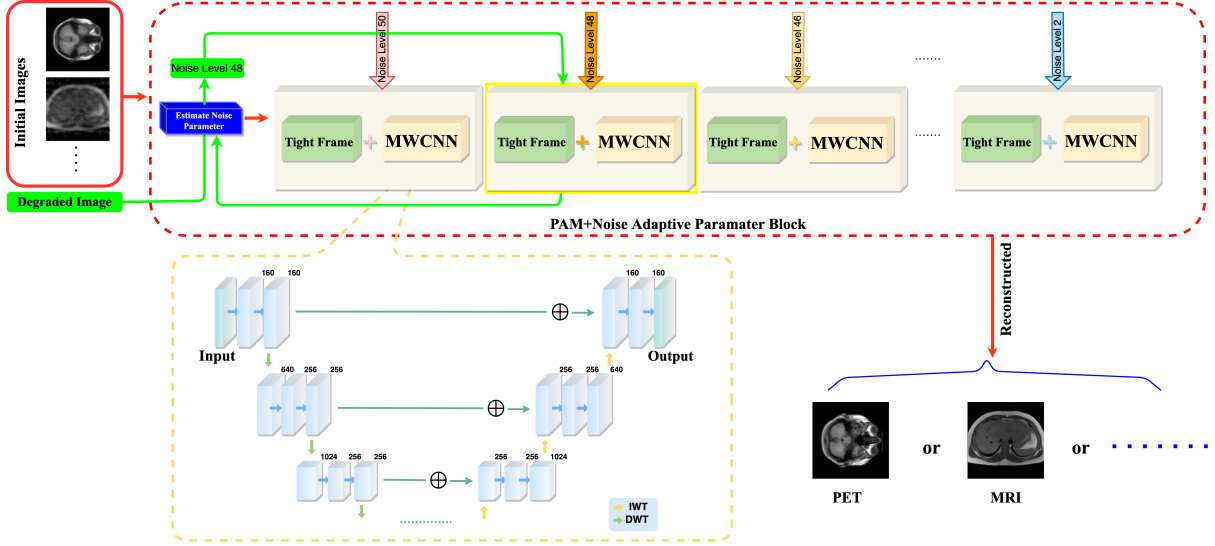
Figure 2. The flowchart of our method. Our method takes degraded data as the input and uses simple methods to calculate the initial value of the iteration, such as IFFT and EM. In each iteration, our algorithm estimates the current noise level to select the specific denoiser. The input of each iteration is calculated through two regularizations: MWCNN and wavelet. The MWCNN network is with a depth of 24 and each CNN block has 4 layers.

sults, as demonstrated alongside state-of-the-art models in Fig. 1. To better reveal the effectiveness of the proposed method, we test both the MRI and PET reconstruction. The handcraft methods (TV [6], the data-driven tight frame (DDTF) [15]), a deep learning method IRCNN [19], the inverse fast Fourier transform (IFFT), and the expectation-maximization (EM) algorithm [18] are considered. From Fig. 1(b) and (c), it can be clearly observed that the results reconstructed by the tight frame method are pretty good compared to the TV model. Compared to Fig. 1(c) and (d), i.e., the tight frame regularizer and the standalone CNN regularizer, the proposed model (Fig. 1(e)) have better results in both MRI and PET reconstruction. The tight frame-based model has shown effective performance in capturing image singularities [28, 29]. The implicit CNN-based regularization can produce deep image priors of the images and describe the fine detail which is hardly captured by the tight frame regularizer. In this work, we intend to combine the MWCNN with tight frame for medical image reconstruction. Fig. 1(e) demonstrates that our new combination is feasible. More detailed results are presented in Section 4. The experiments clearly show that the proposed model has promising performance in various medical imaging tasks. The main contributions are summarized as follows:

- An interpretable medical image reconstruction framework with deep learning-based method is explored. Experiments show that the model trained to denoise Gaussian noise not only works well with Gaussian noise but also with Poisson noise.

- The reconstruction model proposed in this paper is a hybrid scheme, and the PAM algorithm is utilized to solve the proposed model. Meanwhile, the convergence of this scheme is analyzed with numerical results.

- Two challenging medical image reconstruction tasks, MRI and PET, are addressed with multi-noise-level denoiser to demonstrate the robustness of the proposed model. The experimental results demonstrate clearly the superiority of our method over several state-of-the-art methods.

2. Related Works

In this section, we briefly review the traditional tight frame-based techniques and the MWCNN-based schemes.

2.1. Tight Frame Regularizer

The tight frame is a widely used method due to its capability for sparsely approximating piecewise-smooth functions, and the tight frame construction makes the model easy to be tackled [30, 31]. Let $\mathcal{H}$ be a Hilbert space and $\mathbb{Z}$ be the set of integers, a sequence $\{\phi_n : n \in \mathbb{Z}\} \subseteq \mathcal{H}$ is called a tight frame on $\mathcal{H}$ if $\|u\|^2 = \sum_{n \in \mathbb{Z}} |\langle u, \phi_n \rangle|^2$, for all $u \in \mathcal{H}$. The analysis operator W is defined by $W : u \in \mathcal{H} \mapsto \{\langle u, \phi_n \rangle\} \in \ell_2(\mathbb{Z})$. The corresponding synthesis operator is defined by $W^T : \{a_n\} \in \ell_2(\mathbb{Z}) \mapsto \sum_n a_n \phi_n \in \mathcal{H}$. Thus, $\{\phi_n : n \in \mathbb{Z}\}$ is a tight frame on $\mathcal{H}$ if and only if $W^T W = I$, where $I : \mathcal{H} \mapsto \mathcal{H}$ is the identical operator.

Denote $v = (v_1, v_2, \cdots, v_c)$ as the wavelet frame coefficient of the ideal image u under a given tight frame transform W which satisfies $W^T W = I$. The model (1) for image reconstruction can be further revised as follows

$$\min_{W,u,v} \ \Phi(Au, f) + \frac{\mu}{2} \|Wu - v\|_2^2 + \lambda \|v\|_{2,0}, \quad \text{subject to} \ \ W^T W = I, \tag{2}$$

where μ and λ are positive parameters, the $\ell_{2,0}$ norm is a generalization of ℓ_0-norm to vector-valued data and defined as $\|v\|_{2,0} = \sum_{j=1}^c \chi_{v_j \neq 0}$, where $\chi_{v_j \neq 0}$ is the characteristic function of $v_j \neq 0$. The $\|\cdot\|_{2,0}$ encodes the structural correlation among the channel images, which implies the advantages in multichannel image restoration. Interested readers may consult [17] for details.

2.2. MWCNN Regularizer

The MWCNN regularizer [24] can better balance the computational burden and the receptive field size. The MWCNN is an extension of U-Net [32], which includes discrete wavelet transform (DWT), inverse wavelet transform (IWT), and CNN block. We replace the pooling layer with DWT, replace the upsampling layer with IWT, and replace concatenation with elementwise summation. The DWT is used to accelerate the number of feature map channels. With CNN blocks added between any two levels DWTs, wavelet packet transform (WPT) is extended to MWCNN. We obtain training pairs $\{(\mathbf{x_i}, \mathbf{y_i})\}_{i=1}^N$ by adding Gaussian noise into clean images $\mathbf{y_i}$, where $\mathbf{x_i}$ are the noisy images. The loss function of this network is

$$L(\mathbf{\Theta}) = \frac{1}{2N} \sum_{i=1}^N \|G(\mathbf{x_i}; \mathbf{\Theta}) - \mathbf{y_i}\|_2^2,$$

where $\mathbf{\Theta}$ denotes the network parameters, and $G(\mathbf{x_i}; \mathbf{\Theta})$ is the output. The yellow box in the lower left corner of Fig. 2 represents the structure of the MWCNN scheme. We totally trained 25 such models with different noise levels for the proposed model. The 25 denoisers are trained parallelly. The obtained denoisers can be fixed to handle other image processing tasks, such as Cauchy noise removal [25, 33]. On the other hand, the end-to-end network-based approaches are mostly a black box without interpretation. However, as to the medical-related image, the output of the end-to-end network is quite unreliable. In this paper, we refer to the end-to-end deep learning method as the denoiser prior learned directly from the image. While this method remains a black box in terms of its internal decision-making processes, we view the learned information as a deep regularizer. By integrating this deep regularizer into our proposed model, we augment the interpretability of the deep learning-based approach. In our hybrid model, the deep neural network serves as a complementary component alongside traditional mathematical models. Together, they form a comprehensive framework where the deep neural network functions as a deep regularizer. This approach not only enhances the performance of the traditional model but also improves the interpretability of deep learning techniques.

3. The Proposed Model and Algorithm

In this section, the proposed technique is presented. To demonstrate the effectiveness of our method, MRI and PET reconstruction are considered. In addition, the proximal alternating minimization (PAM) algorithm is introduced to handle the proposed hybrid scheme.

3.1. The Proposed Strategy

The proposed medical image reconstruction strategy is given as follows

$$\min_{u,v,W} \ \Phi(Au, f) + \frac{\mu}{2} \|Wu - v\|_2^2 + \lambda \|v\|_{2,0} + \tau R(u), \ \text{subject to} \ W^T W = I. \tag{3}$$

The first term $\Phi(Au, f)$ denotes the data fitting, A is the corresponding acquisition operator, u is the latent image, f is an obtained object; the middle two terms denote the tight frame regularizer, W is the wavelet tight frame and satisfies $W^T W = I$, v represents the wavelet frame coefficient; μ, λ, and τ are positive parameters; and the last term $R(u)$ is a regularizer.

Note that the proposed model (3) is a general framework for image reconstruction. If $R(u) = \|\nabla u\|_1$, the proposed is a total variation (TV) hybrid model, here ∇ is the gradient operator. If $R(u) = \|Da - Eu\|_2^2 + \kappa \|a\|_0$, the proposed is a dictionary learning hybrid model, where D is a learned dictionary, a is the coefficient matrix, E is the extract operator, κ is a positive parameter [34]. To further improve the traditional regularization, our $R(u)$ is an implicit regularizer, whose related subproblem can be treated as a denoiser. Due to the invertibility of DWT and its frequency and location property, MWCNN is effective in recovering detailed textures and sharp structures from degraded observation. Since the tight frame can preserve the edge information, the combination of the tight frame and MWCNN can better restore the degraded image.

Given an observation, firstly, we can estimate the noise level by using the strategy proposed in [35]. According to the result of the noise level estimated, we choose the corresponding denoiser for different image reconstructions. We initially train the deep MWCNN as a denoiser and subsequently plug it into our model as a deep regularizer. The pipeline of our method can be concluded in Fig. 2. The "Tight Frame" and the "MWCNN" blocks represent the tight frame regularizer and the MWCNN regularizer, respectively. Here we give an example as the green line in Fig. 2, if the noise parameter is estimated to be 48, then our method passes through the denoiser with noise level 48. After the iterations, we can have the reconstruction results.

As PET and MRI reconstruction are different tasks, we establish two related medical image reconstruction models and display the solving strategy in the next two subsections.

3.2. Magnetic Resonance Imaging Reconstruction Algorithm

For the MRI reconstruction, let A_1 denote the acquisition process of MRI. By introducing variable z, and the non-negative parameter ξ, our MRI reconstruction model is turned into

$$\min_{u,v,W,z} \ \|A_1 u - f\|_2^2 + \frac{\mu}{2} \|Wu - v\|_2^2 + \lambda \|v\|_{2,0} + \tau R(z) + \frac{\xi}{2} \|u - z\|_2^2, \ \text{subject to} \ W^T W = I. \tag{4}$$

The solution of Eq. (4) should be the exact solution of Eq. (3) when ξ tends to infinity. To derive the solution of model (4), the classical proximal alternating minimization (PAM) algorithm [36] is applied to solve the u, v, W, z in an alternating manner as follows.

- u-subproblem

$$u^{k+1} = \arg \min_{u} \|A_1 u - f\|_2^2 + \frac{\mu}{2} \left\|W^k u - v^k\right\|_2^2 + \frac{\xi}{2} \|u - z^k\|_2^2, \tag{5}$$

then we have

$$(2A_1^T A_1 + \mu(W^k)^T W^k + \xi I)u^{k+1} = 2A_1^T f + \mu(W^k)^T v^k + \xi z^k.$$

The fast Fourier transform (FFT) can be used to find the solution of the above linear system. Since $W^T W = I$, the solution is as follows

$$u^{k+1} = \mathcal{F}^{-1}\left(\frac{2\mathcal{F}(A_1)^* \circ \mathcal{F}(f) + \mu \mathcal{F}(W^k)^* \circ \mathcal{F}(v^k) + \xi \mathcal{F}(z^k)}{2\mathcal{F}(A_1)^* \circ \mathcal{F}(A_1) + \mu + \xi}\right), \tag{6}$$

where $\mathcal{F}$ denotes the two-dimensional discrete Fourier transform, $*$ represents complex conjugation, $\circ$ means component-wise multiplication, and the division is component-wise as well.

- *W*-subproblem

$$W^{k+1} = \arg \min_{W^T W = I} \frac{\mu}{2} \left\| W u^{k+1} - v^k \right\|_2^2 + \frac{\beta^k}{2} \left\| W - W^k \right\|_2^2, \tag{7}$$

where β is a positive parameter, the close-form solution of the above minimization problem is given by

$$W^{k+1} = XY^T, \tag{8}$$

where X, Σ, and Y are the singular value decomposition (SVD) of $u^{k+1}(v^k)^T + \frac{\beta^k}{\mu} W^k$.

- *v*-subproblem

$$v^{k+1} = \arg \min_v \ \lambda \|v\|_{2,0} + \frac{\mu}{2} \left\| v - W^{k+1} u^{k+1} \right\|_2^2 + \frac{\gamma^k}{2} \left\| v - v^k \right\|_2^2, \tag{9}$$

where γ is a positive parameter, the above subproblem can be easily solved by the hard thresholding algorithm [37] as

$$v^{k+1} = \mathcal{T}_{2\lambda, \mu + \gamma^k} \left(\frac{\mu (W^{k+1})^T W^{k+1} + \gamma^k v^k}{\mu I + \gamma^k} \right), \tag{10}$$

where $\mathcal{T}_{\lambda, W}(u)_i = \begin{cases} u_i & \text{if } \sum_{i=1}^{2} w_i |u_i|^2 \geq \lambda, \\ 0 & \text{otherwise.} \end{cases}$

- *z*-subproblem

$$z^{k+1} = \arg \min_z \tau R(z) + \frac{\xi}{2} \|z - u^{k+1}\|_2^2, \tag{11}$$

for *z*-subproblem, we first rewrite Eq. (11) as

$$z^{k+1} = \arg \min_z \ \frac{1}{2(\sqrt{\tau/\xi})^2} \|u^{k+1} - z\|_2^2 + R(z), \tag{12}$$

then we have

$$z^{k+1} = \text{Prox}_{\frac{\tau}{\xi}} R(z - u^{k+1}), \tag{13}$$

where Prox is a proximal operator [38] which can be defined as

$$\text{Prox}_{\frac{\tau}{\xi}} R(z) := \arg \min_u \left\{ R(u) + \frac{1}{2 \cdot \frac{\tau}{\xi}} \|u - z\|_2^2 \right\}. \tag{14}$$

According to Bayes rule, Eq. (12) corresponds to denoising the image u^{k+1} by the MWCNN denoiser with noise level τ/ξ. To address this, we rewrite Eq. (12) as

$$z^{k+1} = \text{Denoiser}(u^{k+1}, \sqrt{\tau/\xi}). \tag{15}$$

3.3. Positron Emission Tomography Reconstruction Algorithm

As to the PET reconstruction, denoting A_2 as the acquisition process operator of PET, our reconstruction model is as follows

$$\min_{u,v,W,z} \ \Phi_1(u) + \frac{\mu}{2} \|Wu - v\|_2^2 + \lambda \|v\|_{2,0} + \tau R(z) + \frac{\xi}{2} \|u - z\|_2^2, \ \text{ subject to } \ W^T W = I, \tag{16}$$

where $\Phi_1(u) = \langle \mathbf{1}, A_2 u + c \rangle - \langle f, \ln(A_2 u + c) \rangle$ is the data fitting term. Similarly, by introducing the parameter α, the PET reconstruction model Eq. (16) can also be solved by the PAM algorithm. Compared with MRI reconstruction, the main difference of PET reconstruction is the *u*-subproblem. And the associated *u*-subproblem of PET can be written as

$$u^{k+1} = \arg \min_u \ \Phi_1(u) + \frac{\mu}{2} \left\| W^k u - v^k \right\|_2^2 + \frac{\xi}{2} \|u - z^k\|_2^2 + \frac{\alpha^k}{2} \left\| u - u^k \right\|_2^2. \tag{17}$$

Algorithm 1 The proposed image reconstruction algorithm

Input:

    Initial image u^0 is obtained by the IFFT with zero filling for MRI reconstruction and by EM algorithm for PET reconstruction;

    Parameter μ, λ;

Output:

    The reconstructed image u;

1: Initialization: $u = u^0$;

2: **for** k=0:N **do**

3:     Evaluate parameters τ and ξ;

4:     Calculate u^{k+1} for MRI reconstruction by Eq. (6) and for PET reconstruction by Eq. (20);

5:     Calculate W^{k+1} by Eq. (8);

6:     Calculate v^{k+1} by Eq. (9);

7:     Calculate z^{k+1} by Eq. (15);

8:     k = k + 1;

9: **end for**

We can use the projected scaled gradient method [39] to solve this problem as

$$u^{k+1} = \arg\min_u \ \Phi_1(u) + \frac{\mu}{2}\left\|W^k u - v^k\right\|_2^2 + \frac{\xi + \alpha^k}{2}\|\sqrt{2}u - \frac{1}{\sqrt{2}}(z^k + u^k)\|_2^2. \tag{18}$$

For $j = 0, 1, 2, ...$, we have

$$M^j = \mathrm{diag}\left(u^j / A_1^T \mathbf{1}\right), \tag{19}$$

$$u^{\frac{j+1}{2}} = u^j - \rho^j M^j\left[A_1^T(\mathbf{1} - \frac{f}{A_1 u^j}) + \mu(u^j - (W^k)^T v^k) + (\xi + \alpha^k)(\sqrt{2}u^j - \frac{1}{\sqrt{2}}(z^k + u^k))\right], \tag{20}$$

$$u^{j+1} = \min\left\{\max\left\{u^{j+1/2}, 0\right\}, a\right\}. \tag{21}$$

Thus, our method can be easily realized with the above equations. The processes of our medical image reconstruction method are shown in Algorithm 1. The algorithm terminates when either the relative difference between consecutive values of the objective function is less than $\epsilon = 1e - 8$, or the number of iterations exceeds $N = 300$.

4. Experiments

    To demonstrate the effectiveness of the proposed reconstruction method, we compare our proposed method with some state-of-the-art methods, including expectation-maximization (EM) algorithm [18], TV [6], DDTF [15], L1-0.5L2 [40], BM3D [41], PANO [42] and deep learning-based method IRCNN [19] and MWCNN [24].

4.1. Training Details

    We choose three datasets to train the networks, i.e. Berkeley Segmentation Dataset[1] (BSD) [43], DIV2K[2] [44], and Waterloo Exploration Database[3] (WED) [45]. We download the images from the dataset mentioned above as a training set and converted these RGB data to grayscale before training. Each image is cropped into patches of size 240×240, totally $24 \times 9,000$ patches for training. We train networks using the MatConvNet package with 4 NVIDIA GTX1080 Ti GPUs on Ubuntu18.04. We train a series of MWCNN with noise levels from 2 to 50 and a step size of 2. Each network is trained by using ADAM algorithm with $\alpha = 1e-2, \beta_1 = 0.9, \beta_2 = 0.999, \epsilon = 1e\text{-}8$ for 10 epochs. We observed that training the network for 10 epochs was sufficient for convergence, a conclusion consistent with similar

---

[1] https://www2.eecs.berkeley.edu/Research/Projects/CS/vision/bsds/
[2] https://data.vision.ee.ethz.ch/cvl/DIV2K/
[3] https://ece.uwaterloo.ca/~k29ma/exploration/

Table 1. PSNR, SSIM, SAM, and NMSE values for MRI reconstruction

Image	PSNR↑									SSIM↑									SAM↓									NMSE↓								
	IFFT	TV	L1L2	BM3D	PANO	DDTF	IRCNN	MWCNN	Ours	IFFT	TV	L1L2	BM3D	PANO	DDTF	IRCNN	MWCNN	Ours	IFFT	TV	L1L2	BM3D	PANO	DDTF	IRCNN	MWCNN	Ours	IFFT	TV	L1L2	BM3D	PANO	DDTF	IRCNN	MWCNN	Ours
M01	20.55	22.11	21.66	22.81	24.10	27.14	29.76	31.01	31.23	0.5992	0.6748	0.7343	0.6788	0.7400	0.8215	0.8468	0.8691	0.8725	0.4002	0.3317	0.2554	0.3056	0.2622	0.1834	0.1356	0.1173	0.1144	0.0939	0.0785	0.0826	0.0724	0.0624	0.0439	0.0325	0.0281	0.0274
M02	20.83	24.93	25.69	26.16	27.47	27.41	28.01	29.15	29.23	0.5192	0.6711	0.7089	0.6982	0.7516	0.7612	0.7683	0.7997	0.8007	0.3222	0.1992	0.1712	0.1733	0.1488	0.1501	0.1399	0.1226	0.1215	0.0909	0.0567	0.0519	0.0492	0.0423	0.0426	0.0397	0.0349	0.0345
M03	21.83	25.91	22.50	28.28	28.20	28.33	29.29	29.76	29.80	0.5419	0.6783	0.6896	0.7393	0.7503	0.7782	0.7845	0.8047	0.8052	0.2795	0.174	0.1551	0.1326	0.1339	0.1319	0.181	0.1119	0.1114	0.0810	0.0506	0.0750	0.0385	0.0389	0.0383	0.0343	0.0325	0.0324
M04	20.88	23.50	23.18	26.68	25.81	26.41	28.81	29.21	29.29	0.5184	0.6473	0.7005	0.7366	0.7275	0.7527	0.8040	0.8083	0.8103	0.3268	0.2391	0.1847	0.1658	0.1836	0.1714	0.1297	0.1239	0.1226	0.0904	0.0668	0.0694	0.0463	0.0513	0.0478	0.0363	0.0347	0.0343
M05	21.88	24.27	24.43	28.48	28.79	29.66	31.04	31.59	31.81	0.5619	0.6178	0.7242	0.7479	0.7839	0.8246	0.8423	0.8597	0.8626	0.2718	0.2065	0.1536	0.1269	0.1224	0.1108	0.0944	0.0886	0.0864	0.0805	0.0612	0.0601	0.0377	0.0364	0.0329	0.0281	0.0263	0.0257
M06	20.73	22.48	23.33	23.57	24.24	24.23	25.30	26.33	26.69	0.5318	0.5805	0.6263	0.6364	0.6512	0.6484	0.6768	0.7201	0.7257	0.2958	0.2407	0.2148	0.2125	0.1965	0.1966	0.1736	0.1540	0.1477	0.0919	0.0751	0.0681	0.0663	0.0614	0.0543	0.0489	0.0482	0.0463
M07	21.27	23.91	26.21	26.86	26.62	28.04	29.63	30.12	30.41	0.5441	0.6886	0.7301	0.7501	0.7595	0.7992	0.8219	0.8365	0.8439	0.3059	0.2245	0.1695	0.1598	0.1643	0.1394	0.1160	0.1096	0.1059	0.0864	0.0638	0.0489	0.0454	0.0466	0.0396	0.0330	0.0312	0.0302
M08	21.98	26.28	26.75	27.75	27.44	28.17	29.10	29.97	30.11	0.5204	0.7679	0.7598	0.7615	0.7713	0.8156	0.8248	0.8451	0.8473	0.2957	0.1791	0.1668	0.1514	0.1571	0.1444	0.1296	0.1172	0.1153	0.0796	0.0485	0.0460	0.0410	0.0425	0.0390	0.0351	0.0317	0.0312
M09	21.98	23.28	24.68	24.06	24.99	25.41	26.19	27.20	27.17	0.5150	0.6215	0.6618	0.6257	0.6678	0.6917	0.7037	0.7434	0.7410	0.2984	0.2236	0.1875	0.2048	0.1837	0.1752	0.1599	0.1422	0.1427	0.0908	0.0686	0.0583	0.0627	0.0563	0.0537	0.0490	0.0436	0.0438
M10	20.90	24.20	25.29	26.00	26.24	27.73	28.42	29.23	29.34	0.6417	0.6660	0.7132	0.7238	0.7252	0.7501	0.7649	0.7844	0.7870	0.2739	0.1868	0.1482	0.1529	0.1485	0.1251	0.1155	0.1052	0.1039	0.0901	0.0616	0.0544	0.0501	0.0488	0.0411	0.0379	0.0345	0.0341
M11	19.90	23.12	25.01	23.48	25.01	25.55	26.32	26.46	27.26	0.5421	0.6038	0.6653	0.6322	0.6699	0.6863	0.7045	0.7210	0.7391	0.3156	0.2161	0.1735	0.2084	0.1744	0.1639	0.1497	0.1475	0.1344	0.1012	0.0698	0.0562	0.0670	0.0562	0.0528	0.0483	0.0476	0.0434
M12	21.10	23.96	26.10	25.23	26.87	28.07	28.55	30.76	31.00	0.5678	0.6556	0.7191	0.6904	0.7517	0.8036	0.7956	0.8415	0.8461	0.2997	0.2137	0.1671	0.1850	0.1527	0.133	0.1259	0.0975	0.0948	0.0882	0.0634	0.0495	0.0548	0.0454	0.0395	0.0374	0.0290	0.0282
M13	20.58	23.34	24.15	25.92	26.94	27.64	28.18	28.99	29.15	0.5796	0.6479	0.7266	0.7214	0.7567	0.7771	0.7847	0.8065	0.8117	0.3165	0.2293	0.1659	0.1707	0.1515	0.1398	0.1313	0.1196	0.1173	0.0936	0.0681	0.0492	0.0506	0.0450	0.0415	0.0390	0.0355	0.0349
M14	21.51	24.05	22.54	25.41	26.22	26.37	26.77	28.01	28.22	0.5294	0.6539	0.6757	0.6751	0.7221	0.7346	0.7253	0.7724	0.7778	0.2969	0.2199	0.1871	0.1886	0.1717	0.1688	0.1610	0.1396	0.1362	0.0840	0.0627	0.0747	0.0536	0.0489	0.0480	0.0459	0.0398	0.0388
M15	21.25	24.40	23.18	25.58	26.93	26.77	27.72	28.49	28.59	0.5315	0.7091	0.7212	0.6924	0.7596	0.7795	0.7847	0.8008	0.7988	0.3091	0.2128	0.1747	0.1865	0.1593	0.1625	0.1456	0.1332	0.1317	0.0866	0.0603	0.0694	0.0526	0.0450	0.0458	0.0411	0.0376	0.0372
Ave.	21.07	23.98	24.45	25.75	26.39	27.13	28.21	29.09	29.29	0.5496	0.6589	0.7038	0.7006	0.7326	0.7616	0.7755	0.8009	0.8046	0.3072	0.2198	0.1783	0.1817	0.1674	0.1531	0.1351	0.1220	0.1191	0.0886	0.0637	0.0609	0.0525	0.0485	0.0445	0.0395	0.0357	0.0348
M16	22.04	26.26	27.26	29.80	29.08	29.59	29.84	29.69	30.06	0.4951	0.8327	0.8158	0.9060	0.8621	0.9196	0.9190	0.9120	0.9116	0.3845	0.2346	0.1889	0.1561	0.1697	0.1600	0.1555	0.1582	0.1516	0.0791	0.0487	0.0434	0.0324	0.0352	0.0332	0.0322	0.0328	0.0314
M17	22.27	27.13	28.99	30.51	29.88	30.44	30.66	31.16	31.58	0.5308	0.8420	0.8203	0.8970	0.8565	0.8999	0.9097	0.9111	0.9098	0.3759	0.2245	0.1805	0.1527	0.1641	0.1539	0.1501	0.1416	0.1349	0.0729	0.0440	0.0355	0.0298	0.0321	0.0301	0.0293	0.0277	0.0264
M18	22.01	25.50	28.40	30.60	29.41	30.16	30.13	30.91	31.25	0.5003	0.7218	0.8077	0.9066	0.8653	0.9077	0.9080	0.9141	0.9153	0.4019	0.2649	0.1909	0.1478	0.1694	0.1556	0.1562	0.1427	0.1370	0.0793	0.0531	0.0380	0.0295	0.0338	0.0311	0.0312	0.0285	0.0274
M19	21.33	22.69	26.29	29.21	28.05	28.79	30.30	30.30	30.55	0.4959	0.7561	0.7593	0.8816	0.8428	0.8982	0.9105	0.9062	0.9044	0.4148	0.3522	0.2207	0.1643	0.1880	0.1728	0.1451	0.1449	0.1408	0.0858	0.0734	0.0485	0.0346	0.0396	0.0364	0.0306	0.0305	0.0297
M20	23.53	26.38	26.81	29.60	29.17	29.56	29.85	30.01	30.25	0.5289	0.7306	0.7317	0.8124	0.7907	0.8405	0.8418	0.8396	0.8409	0.3511	0.2514	0.2045	0.1735	0.1823	0.1742	0.1685	0.1655	0.1608	0.0666	0.0480	0.0456	0.0331	0.0348	0.0333	0.0322	0.0316	0.0307
M21	22.37	24.24	26.33	26.89	26.27	26.63	27.07	27.46	27.88	0.4846	0.6828	0.6032	0.7701	0.7134	0.7962	0.8042	0.7799	0.8059	0.3259	0.2617	0.2053	0.1922	0.2065	0.1982	0.1883	0.1800	0.1714	0.0761	0.0614	0.0483	0.0452	0.0486	0.0466	0.0443	0.0424	0.0404
M22	23.56	25.47	26.15	29.66	29.25	29.99	30.99	31.61	32.38	0.5355	0.7676	0.7485	0.8525	0.8248	0.8912	0.8983	0.8888	0.8995	0.3622	0.2892	0.2211	0.1775	0.1859	0.1710	0.1522	0.1417	0.1295	0.0664	0.0533	0.0493	0.0329	0.0345	0.0317	0.0282	0.0263	0.0240
M23	22.51	24.88	26.87	30.39	29.13	29.79	29.81	31.42	31.73	0.5091	0.8136	0.7632	0.9194	0.8710	0.9166	0.9180	0.9297	0.9289	0.4108	0.3096	0.2244	0.1630	0.1888	0.1749	0.1745	0.1447	0.1396	0.0749	0.0570	0.0453	0.0302	0.0350	0.0324	0.0323	0.0269	0.0259
M24	22.29	24.79	25.18	28.22	27.61	28.04	28.61	28.71	29.05	0.4797	0.7645	0.7242	0.8440	0.8038	0.8651	0.8704	0.8571	0.8708	0.3648	0.2720	0.2219	0.1827	0.1961	0.1867	0.1747	0.1727	0.1659	0.0768	0.0576	0.0551	0.0388	0.0416	0.0396	0.0371	0.0367	0.0353
M25	22.23	23.91	25.16	26.61	26.00	26.48	27.27	27.37	27.41	0.4822	0.6814	0.6584	0.7617	0.7161	0.7921	0.8020	0.8092	0.8086	0.3335	0.2720	0.2190	0.2144	0.1999	0.2030	0.1850	0.1828	0.1821	0.0773	0.0637	0.0552	0.0467	0.0501	0.0474	0.0433	0.0428	0.0426
M26	21.56	23.16	24.04	26.02	25.53	26.17	26.73	27.54	27.90	0.4709	0.6634	0.6345	0.7674	0.6999	0.7929	0.7973	0.8169	0.8246	0.3594	0.2978	0.2528	0.2131	0.2255	0.2095	0.1963	0.1786	0.1712	0.0835	0.0695	0.0628	0.0500	0.0529	0.0491	0.0461	0.0420	0.0403
M27	22.91	25.01	27.34	27.86	27.29	28.00	28.02	28.48	28.77	0.5003	0.6910	0.6146	0.7787	0.7268	0.8018	0.8004	0.7975	0.8136	0.3303	0.2580	0.1970	0.1854	0.1980	0.1824	0.1821	0.1727	0.1668	0.0715	0.0561	0.0429	0.0404	0.0432	0.0398	0.0397	0.0377	0.0364
M28	21.64	23.51	24.60	25.68	25.09	25.65	25.72	25.69	25.85	0.4265	0.6827	0.6311	0.7827	0.6972	0.7846	0.7755	0.7860	0.7778	0.3397	0.2741	0.2416	0.2127	0.2280	0.2136	0.2118	0.2124	0.2087	0.0828	0.0667	0.0589	0.0520	0.0557	0.0522	0.0518	0.0519	0.0510
M29	21.84	23.09	27.12	27.89	26.85	27.22	28.25	28.38	28.95	0.4710	0.5349	0.6336	0.8186	0.7469	0.8323	0.8261	0.8246	0.8462	0.2204	0.1905	0.1197	0.1095	0.1234	0.1183	0.1050	0.1034	0.0969	0.0809	0.0700	0.0441	0.0403	0.0455	0.0435	0.0387	0.0381	0.0357
M30	22.55	26.18	27.26	28.54	28.06	28.36	28.35	28.46	28.59	0.4312	0.7463	0.7809	0.8482	0.7913	0.8338	0.8390	0.8334	0.8287	0.2274	0.1515	0.1244	0.1153	0.1219	0.1178	0.1179	0.1164	0.1147	0.0746	0.0491	0.0433	0.0374	0.0395	0.0382	0.0382	0.0378	0.0372
Ave.	22.34	24.81	26.52	28.50	27.78	28.32	28.77	29.15	29.48	0.4895	0.7274	0.7151	0.8365	0.7872	0.8515	0.8547	0.8537	0.8591	0.3468	0.2604	0.2019	0.1697	0.1841	0.1728	0.1642	0.1572	0.1515	0.0766	0.0581	0.0477	0.0382	0.0415	0.0390	0.0370	0.0356	0.0343

(a) IFFT (19.90/0.5421)   (b) DDTF (25.55/0.6863)   (c) MWCNN (27.15/0.7367)   (d) Ours (27.26/0.7391)

(a) EM (27.85/0.8223)   (b) DDTF (32.17/0.9228)   (c) MWCNN (32.68/0.9199)   (e) Ours (32.97/0.9202)

Figure 3. Reconstruction results (PSNR/SSIM). The first row is the MRI reconstruction results of image 'M11', the second row is the PET reconstruction results of image 'P08'. (a) IFFT and EM [18]; (b) DDTF [15]; (c) MWCNN [24]; (d) Ours.

studies, such as the one referenced in [25]. Regarding the utilization of medical images for training, we acknowledge the potential benefits of training the MWCNN on medical images, which may share similar characteristics such as noise patterns, contrast, and object size. However, it's important to note the scarcity of large medical image datasets suitable for training deep neural networks. We recognize the importance of this avenue for future research and will devote efforts to training the neural network on medical image data.

IRCNN was proposed by [19] to tackle image restoration tasks. Since IRCNN achieved very promising restoration results, we set the IRCNN method as one of our benchmarks. In this paper, the IRCNN network was implemented with MatConvNet toolbox and an NVIDIA GeForce RTX 2080Ti. Note that we did not retrain the IRCNN[4]. The IRCNN collected a large dataset which includes 400 BSD images, 400 selected images from validation set of ImageNet database [46] and 4,744 images of WED. While fine-tuning IRCNN on the same dataset as our proposed method would indeed facilitate a fairer comparison, the datasets covered by both methods substantially overlap. Given this overlap, we anticipate that fine-tuning IRCNN on our selected datasets would yield results comparable to those reported in the paper.

---

[4] https://github.com/cszn/ircnn

Table 2. PSNR, SSIM, SAM, and NMSE values for PET reconstruction

| Image	PSNR↑						SSIM↑						SAM↓						NMSE↓					
	EM	TV	DDTF	IRCNN	MWCNN	Ours	EM	TV	DDTF	IRCNN	MWCNN	Ours	EM	TV	DDTF	IRCNN	MWCNN	Ours	EM	TV	DDTF	IRCNN	MWCNN	Ours
P01	27.07	30.62	31.38	31.37	31.61	**31.78**	0.8097	0.8999	0.9042	0.9001	0.9008	**0.9082**	0.1521	0.1007	0.0925	0.0927	0.0901	**0.0883**	0.0443	0.0294	0.0270	0.0270	0.0263	**0.0257**
P02	28.08	31.83	32.8	32.71	32.96	**33.28**	0.8172	0.9087	0.9157	0.9070	0.9087	**0.9184**	0.1538	0.0998	0.0893	0.0903	0.0878	**0.0845**	0.0394	0.0256	0.0229	0.0231	0.0225	**0.0217**
P03	28.34	31.92	32.82	32.85	32.82	**33.15**	0.8285	0.9096	0.9159	0.9112	0.9068	**0.9178**	0.1547	0.1026	0.0924	0.0920	0.0925	**0.0890**	0.0383	0.0253	0.0228	0.0228	0.0229	**0.0220**
P04	28.00	31.41	32.71	32.65	32.85	**33.09**	0.8274	0.9207	0.9272	0.9183	0.9204	**0.9289**	0.1522	0.1017	0.0886	0.0892	0.0873	**0.0849**	0.0398	0.0269	0.0231	0.0233	0.0228	**0.0222**
P05	27.61	31.08	32.71	32.69	33.10	**33.34**	0.8251	0.9252	0.9345	0.9242	0.9319	**0.9404**	0.1505	0.1000	0.0831	0.0841	0.0802	**0.0780**	0.0417	0.0279	0.0230	0.0232	0.0221	**0.0215**
P06	28.41	31.85	33.04	33.08	33.25	**33.65**	0.8311	0.9174	0.9343	0.9224	0.9295	**0.9383**	0.1406	0.0945	0.0825	0.0822	0.0806	**0.0770**	0.0380	0.0255	0.0223	0.0222	0.0217	**0.0208**
P07	28.15	30.39	32.04	32.30	32.56	**32.76**	0.8256	0.9047	0.9170	0.9147	0.9170	**0.9234**	0.1347	0.0967	0.0861	0.0836	0.0811	**0.0792**	0.0391	0.0302	0.0250	0.0243	0.0235	**0.0230**
P08	27.85	31.08	32.17	32.36	32.61	**32.97**	0.8223	0.9140	0.9228	0.9172	0.9199	**0.9302**	0.1288	0.0889	0.0782	0.0766	0.0744	**0.0714**	0.0405	0.0279	0.0246	0.0241	0.0234	**0.0225**
P09	27.88	29.48	32.23	32.37	32.79	**33.00**	0.8231	0.8870	0.9269	0.9185	0.9257	**0.9344**	0.1317	0.0991	0.0798	0.0785	0.0748	**0.0730**	0.0404	0.0336	0.0245	0.0241	0.0229	**0.0224**
P10	27.67	28.24	31.99	32.29	32.57	**32.72**	0.8335	0.8713	0.9275	0.9233	0.9289	**0.9338**	0.1338	0.1181	0.0813	0.0786	0.0760	**0.0747**	0.0414	0.0387	0.0251	0.0243	0.0235	**0.0231**
P11	27.78	30.18	32.45	32.47	32.83	**33.16**	0.8371	0.9044	0.9359	0.9258	0.9332	**0.9417**	0.1291	0.0912	0.0754	0.0752	0.0722	**0.0695**	0.0408	0.0310	0.0239	0.0238	0.0228	**0.0220**
P12	27.91	30.05	32.81	32.49	33.00	**33.35**	0.8448	0.9091	0.9455	0.9307	0.9399	**0.9491**	0.1222	0.0855	0.0694	0.0721	0.0679	**0.0652**	0.0402	0.0314	0.0229	0.0238	0.0224	**0.0215**
P13	28.46	30.41	33.54	33.15	33.81	**34.18**	0.8572	0.9057	0.9488	0.9343	0.9464	**0.9544**	0.1158	0.0842	0.0645	0.0675	0.0626	**0.0599**	0.0378	0.0302	0.0210	0.0220	0.0204	**0.0196**
P14	28.34	32.05	31.39	32.71	33.25	**33.30**	0.8761	0.9358	0.9296	0.9391	0.9485	**0.9493**	0.1146	0.0740	0.0807	0.0693	0.0651	**0.0647**	0.0383	0.0250	0.0269	0.0232	0.0217	**0.0216**
P15	28.39	32.10	32.73	32.31	32.88	**33.11**	0.8983	0.9472	0.9519	0.9468	0.9526	**0.9548**	0.112	0.0731	0.0680	0.0714	0.0669	**0.0651**	0.0381	0.0248	0.0231	0.0242	0.0227	**0.0221**
Ave.	28.00	30.85	32.46	32.52	32.86	**33.12**	0.8371	0.9107	0.9292	0.9222	0.9273	**0.9349**	0.1351	0.0940	0.0808	0.0802	0.0773	**0.0750**	0.0399	0.0289	0.0239	0.0237	0.0228	**0.0221**
P16	33.78	34.02	37.58	36.99	37.56	**37.88**	0.9560	0.9434	0.9739	0.9663	0.9727	**0.9767**	0.1018	0.0925	0.0657	0.0704	0.0658	**0.0635**	0.0205	0.0199	0.0132	0.0141	0.0132	**0.0128**
P17	34.02	35.59	38.56	37.65	38.43	**38.66**	0.9498	0.9599	0.9773	0.9710	0.9757	**0.9775**	0.1280	0.0971	0.0758	0.0842	0.0770	**0.0750**	0.0199	0.0166	0.0118	0.0131	0.0120	**0.0117**
P18	36.42	35.12	40.17	39.10	40.02	**40.52**	0.9611	0.9402	0.9752	0.9671	0.9757	**0.9789**	0.1200	0.1194	0.0779	0.0882	0.0792	**0.0748**	0.0151	0.0175	0.0098	0.0111	0.0100	**0.0094**
P19	33.98	36.07	38.28	37.52	38.25	**38.57**	0.9603	0.9577	0.9772	0.9696	0.9769	**0.9805**	0.1122	0.0860	0.0685	0.0747	0.0687	**0.0663**	0.0200	0.0157	0.0122	0.0133	0.0122	**0.0118**
P20	36.09	39.45	40.17	39.08	40.03	**40.42**	0.9528	0.9697	0.9725	0.9660	0.9711	**0.9741**	0.1353	0.0910	0.0846	0.0960	0.0860	**0.0822**	0.0157	0.0107	0.0098	0.0111	0.0100	**0.0095**
P21	36.26	37.52	40.99	39.78	41.04	**41.51**	0.9537	0.9656	0.9787	0.9708	0.9791	**0.9820**	0.1361	0.0979	0.0792	0.0910	0.0786	**0.0745**	0.0154	0.0133	0.0089	0.0103	0.0089	**0.0084**
P22	36.76	36.53	40.72	39.87	40.67	**41.13**	0.9590	0.9573	0.9753	0.9714	0.9749	**0.9787**	0.1375	0.1096	0.0873	0.0960	0.0877	**0.0832**	0.0145	0.0149	0.0092	0.0102	0.0093	**0.0088**
P23	35.77	36.58	40.44	39.34	40.36	**40.95**	0.9493	0.9529	0.9751	0.9683	0.9750	**0.9784**	0.1372	0.1123	0.0804	0.0910	0.0809	**0.0756**	0.0163	0.0148	0.0095	0.0108	0.0096	**0.0090**
P24	34.04	30.79	38.47	37.34	38.38	**38.55**	0.9534	0.9363	0.9796	0.9719	0.9789	**0.9801**	0.1103	0.1207	0.0661	0.0754	0.0669	**0.0656**	0.0199	0.0289	0.0119	0.0136	0.0121	**0.0118**
P25	35.39	37.73	40.58	39.24	40.34	**40.74**	0.9529	0.9690	0.9789	0.9704	0.9775	**0.9797**	0.1259	0.0824	0.0692	0.0808	0.0712	**0.0680**	0.0170	0.0130	0.0094	0.0109	0.0096	**0.0092**
P26	36.46	39.00	40.94	39.44	40.65	**41.02**	0.9649	0.9634	0.9804	0.9692	0.9775	**0.9807**	0.1193	0.0890	0.0713	0.0848	0.0738	**0.0707**	0.0150	0.0112	0.0090	0.0107	0.0093	**0.0089**
P27	36.35	36.67	41.35	40.19	41.38	**42.14**	0.9637	0.9641	0.9800	0.9744	0.9815	**0.9849**	0.1132	0.0788	0.0639	0.0728	0.0635	**0.0583**	0.0152	0.0147	0.0086	0.0098	0.0085	**0.0078**
P28	34.84	37.82	39.04	38.28	39.22	**39.58**	0.9497	0.9691	0.9743	0.9699	0.9745	**0.9766**	0.1253	0.0833	0.0774	0.0840	0.0756	**0.0726**	0.0181	0.0128	0.0112	0.0122	0.0109	**0.0105**
P29	36.59	37.36	40.96	39.69	41.17	**41.41**	0.9655	0.9551	0.9774	0.9685	0.9795	**0.9817**	0.1224	0.0972	0.0741	0.0856	0.0722	**0.0702**	0.0148	0.0136	0.0090	0.0104	0.0087	**0.0085**
P30	35.00	38.87	39.95	38.82	39.89	**40.36**	0.9538	0.9733	0.9789	0.9730	0.9790	**0.9808**	0.1310	0.0841	0.0743	0.0845	0.0747	**0.0708**	0.0178	0.0114	0.0101	0.0115	0.0101	**0.0096**
Ave.	35.45	36.61	39.88	38.82	39.83	**40.23**	0.9564	0.9585	0.9770	0.9699	0.9766	**0.9794**	0.1237	0.0961	0.0744	0.0839	0.0748	**0.0714**	0.0170	0.0153	0.0102	0.0115	0.0103	**0.0098**
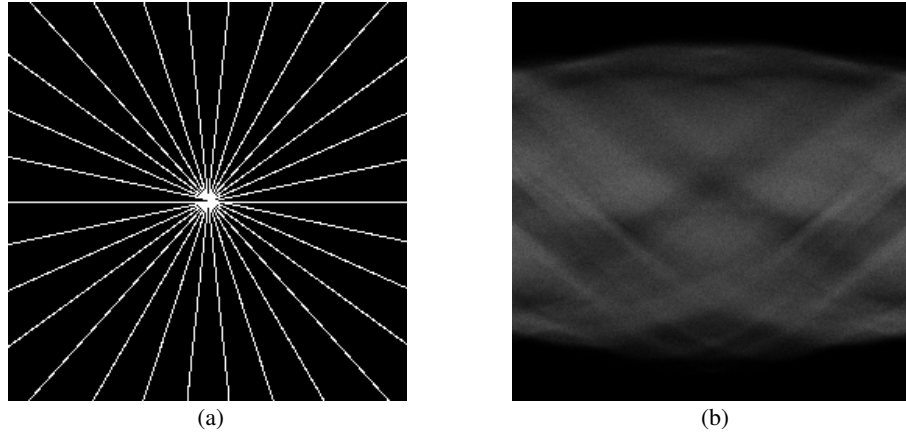
Figure 4. Synthesized data: (a) the radial sampling projection of MRI; (b) synthesized PET data ('P05').
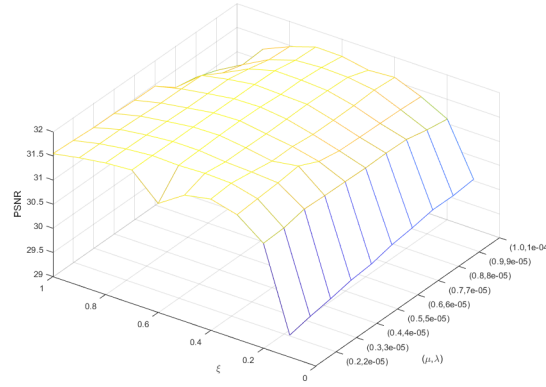
Figure 5. The PSNR values of the PET image 'P01' reconstructed by the proposed model with respect to parameters (μ, λ) and τ.

4.2. Parameter Setting

For PET reconstruction, we test the proposed method on 30 real images, in which 15 images (P1-P15) from brainweb[5] [47] and 15 images (P16-P30) from OASIS[6]. For the test set of MRI reconstruction, we synthesize the downsampled observed data from 15 real MRI images (M1-M15) from cardiacatlas[7] [48] which is a complete labeled MRI image set of one normal patient's heart, and another 15 real images (M16-M30) from OASIS[8]. Synthetic data is popular, and many works applied simulation data for image processing [49]. The synthetic data is considered valid, but it may deviate slightly from the real data. Some indicators (PSRN, SSIM [50], NMSE [51], SAM [52]) are used to measure the quality of the reconstruction results. The definitions are as follows

$$\text{PSNR}(x, y) = 20 \log_{10} \frac{255}{\frac{1}{mn} \|x - y\|_2}, \quad \text{SSIM}(x, y) = \frac{\left(2\mu_x\mu_y + c_1\right)\left(2\sigma_{xy} + c_2\right)}{\left(\mu_x^2 + \mu_y^2 + c_1\right)\left(\sigma_x^2 + \sigma_y^2 + c_2\right)}, \tag{22}$$

$$\text{NMSE}(x, y) = \frac{\|x - y\|_2^2}{\|x\|_2^2}, \quad \text{SAM}(x, y) = \cos^{-1}\left(\frac{y^T x}{\sqrt{(x)^T x^*} \sqrt{y^T y}}\right), \tag{23}$$

---

[5] https://brainweb.bic.mni.mcgill.ca/brainweb/

[6] 15 real PET images are selected from https://www.oasis-brains.org/, which are real PET images of 5 patients.

[7] https://www.cardiacatlas.org/studies/amrg-cardiac-atlas/

[8] 15 real MRI images are selected from https://www.oasis-brains.org/, which are real MRI images of 5 patients. All the test PET and MRI images are collected in https://github.com/Huang-chao-yan/PnP_PAM.

where x and y denote the restored image and the original image; and $\mu_x, \mu_y, \sigma_x^2, \sigma_y^2, \sigma_{x,y}$ are the average, the variance, and the covariance of x and y, respectively, and c_1, c_2 are two constants. Note that larger PSNR, larger SSIM, smaller NMSE, and smaller SAM values indicate better restored results.
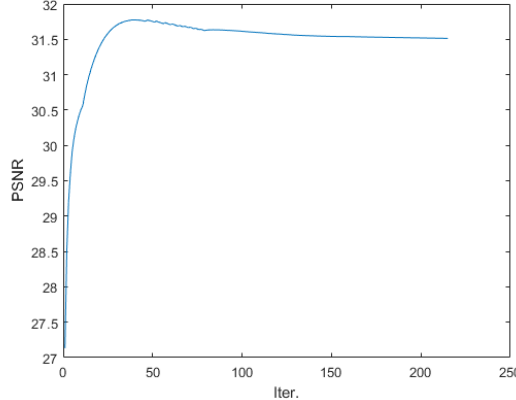
Figure 6. The PSNR curves of the proposed algorithm on PET image 'P01'.

| (a) distribution of MRI results | (b) distribution of PET results | (c) difference of MRI results | (d) difference of PET results |
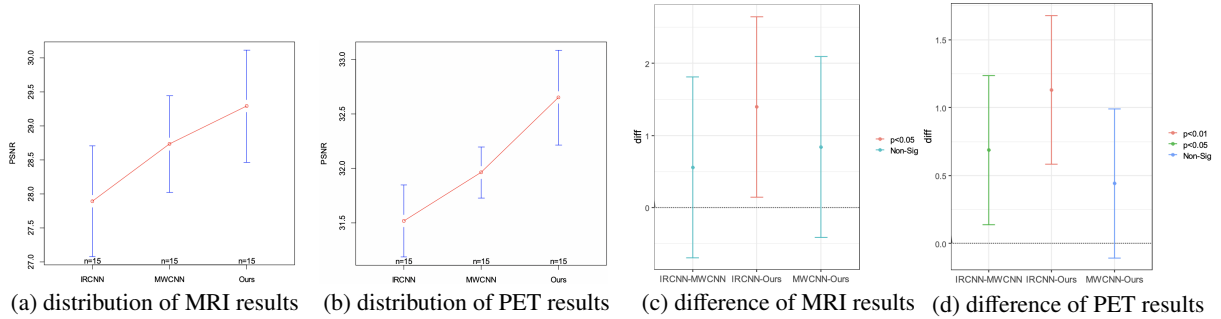
Figure 7. Analysis of variance with five random initial values. (a) the distribution of MRI results with three methods, the red circle is the average of 15 images; (b) the distribution of PET results with three methods, the red circle is the average of 15 images; (c) difference of two different methods of MRI results; (d) difference of two different methods of PET results; here p is the probability, Non-Sig represents the two methods are non-significant.

Usually the hyperparameters need to be tested on the validation set. We get the parameters on the fastMRI Dataset[9] [53]. The architecture of IRCNN, MWCNN, and the proposed method are exactly the same. We choose different hyperparameters by trial and error to produce our best possible result. More specifically, we set $N = 200$, $\alpha^k = 1e{-}2, \beta^k = 5e{-}5, \gamma^k = 5e{-}5, \xi \in (0, 1), \lambda \in (1e{-}5, 1e{-}4)$, and $\mu \in (0, 1)$.

The parameters of other methods are the default values or the corresponding values described in their paper and codes. The radial sampling projection of MRI and the synthesized PET data f are described in Fig. 4. Note that every mask of PET data is not the same, we just depict an example of PET image 'P05'.

We utilize the Matlab built-in function 'imnoise' to add Poisson noise into PET images as follows

$$f = s*\text{imnoise}(A_2 u/s, \text{'Poisson'}),$$

where s indicates noise intensity, A_2 is the PET sample operator, and u is a clean image. In our all experiments, we set s to be $1e9$. Following the setting of literature [54], in this paper, the initial setting of W is the 8×8 Haar wavelet.

---

[9] https://fastmri.med.nyu.edu/

(a) IFFT   (b) TV   (c) L1-0.5L2   (d) BM3D

(a) 20.55/0.5992   (b) 22.11/0.6748   (c) 21.66/0.7343   (d) 22.81/0.6788

(e) PANO   (f) DDTF   (g) IRCNN   (h) Ours

(e) 24.10/0.7400   (f) 27.14/0.8215   (g) 29.76/0.8468   (h) 31.23/0.8725
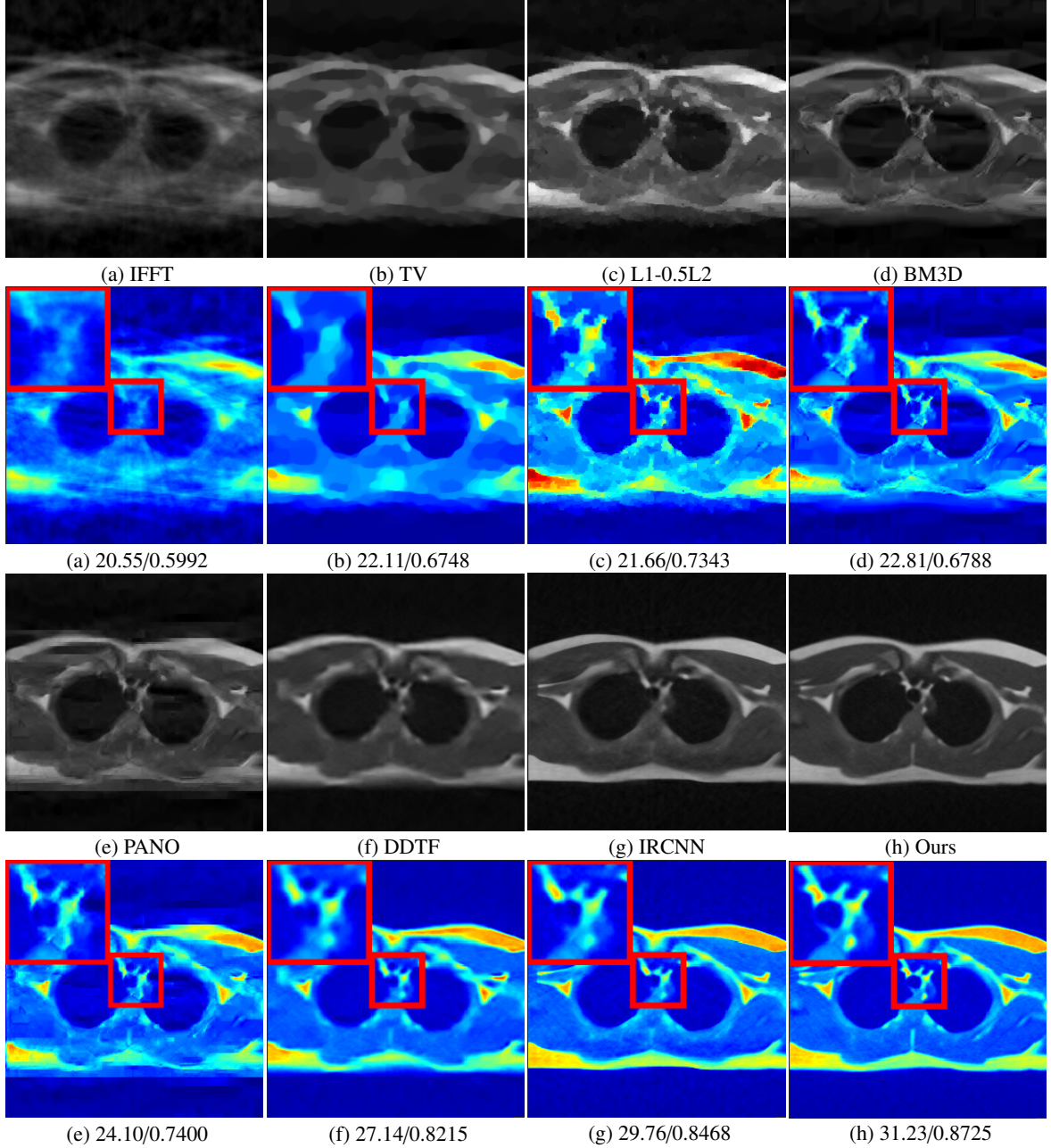
Figure 8. MRI reconstruction results (PSNR/SSIM) of Image 'M01'. (a) the initial image; the reconstructed image by: (b) TV [6]; (c) L1-0.5L2 [40]; (d) BM3D [41]; (e) PANO [42]; (f) DDTF [15]; (g) IRCNN [19]; (h) Ours.

4.3. Contribution of Different Terms

To estimate the distinct contributions of these two regularizers, i.e., the tight frame prior and the deep image prior, we test the reconstruction results of tight frame (only the tight frame regularizer), MWCNN (only the implicit MWCNN regularizer), and the proposed model (both the tight frame and the implicit MWCNN regularizers). Rewriting our model (3) as

$$\min_{u,v,W,z} \Phi(Au, f) + \frac{\mu}{2\lambda}(\|Wu - v\|_2^2 + \|v\|_{2,0}) + \tau R(z), \quad \text{subject to} \quad W^T W = I. \tag{24}$$

13

(a) IFFT (20.44) (b) MWCNN (23.22) (a) Ours (23.71)
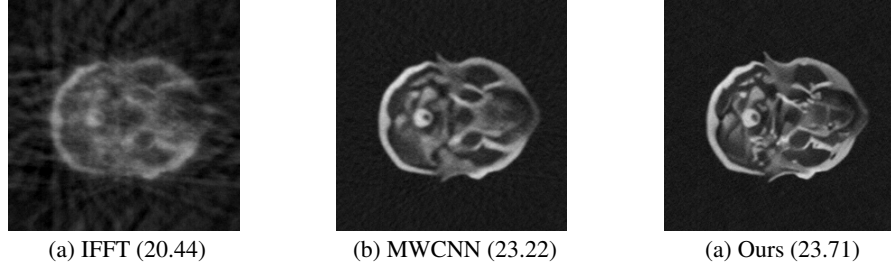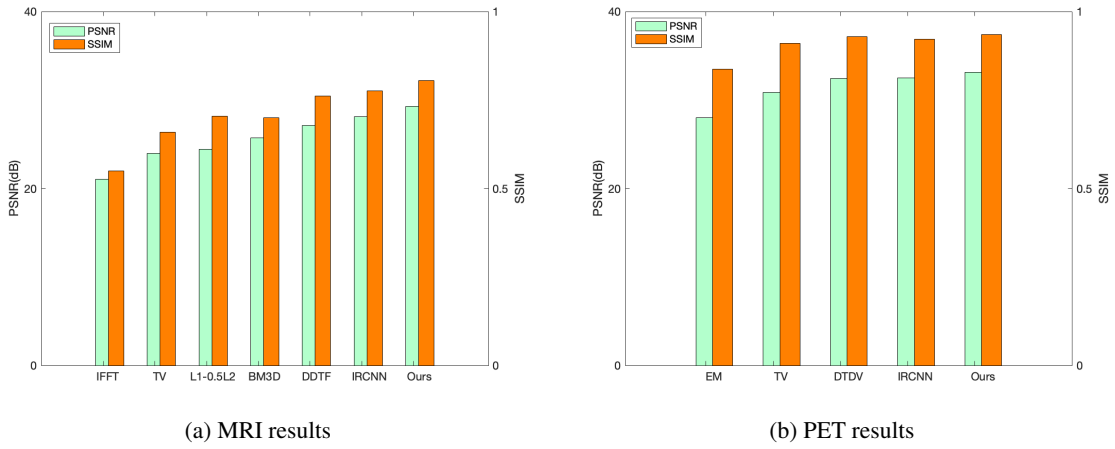
Figure 9. Reconstruction result (PSNR) with Rician noise, the noise level is set to be 0.08. (a) the initial image; the reconstructed image by (b) MWCNN and (c) Ours.

(a) MRI results (b) PET results

Figure 10. The average results of different methods for MRI and PET reconstruction.

When the parameter $\frac{\mu}{2\lambda}$ goes to zero, the model (24) becomes the MWCNN-based model. When the parameter τ goes to zero, the model (24) becomes the tight frame-based model. We give the results of the tight frame-based model, MWCNN-based model, and the proposed model in Fig. 3(b), (c), and (d), respectively. The first row presents the reconstruction results of MRI, and the second row is the results of PET. From both PET and MRI results, we find that the proposed model with both tight frame and MWCNN regularizers achieves better results. In Fig. 5, we also discuss the influence of positive parameters $\frac{\mu}{2\lambda}$ and τ.

4.4. Convergence Behaviour

The convergence of the Plug-and-Play framework with properly trained denoiser has been discussed in [55]. However, the convergence of deep learning-based methods is still an open question. Fig. 6 display the PSNR (dB) curves of the proposed algorithm with the PET image 'P01'. We can obviously observe the numerical convergence of our algorithm.

(a) IFFT	(b) TV	(c) L1-0.5L2	(d) BM3D
(a) 19.90/0.5421	(b) 23.12/0.6038	(c) 25.01/0.6653	(d) 23.48/0.6322
(e) PANO	(f) DDTF	(g) IRCNN	(h) Ours
(e) 25.01/0.6699	(f) 25.55/0.6863	(g) 26.32/0.7045	(h) 27.26/0.7391
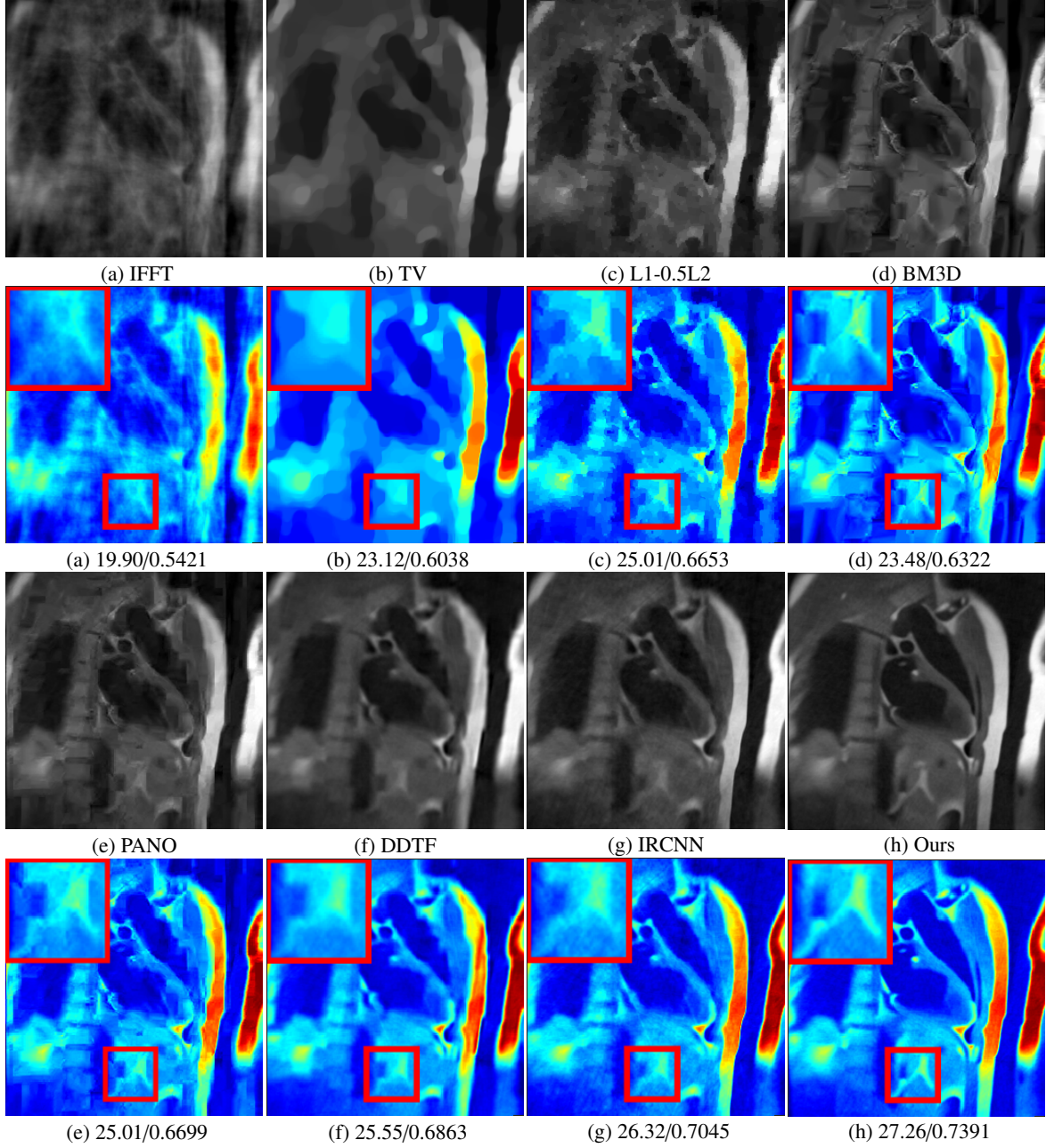
Figure 11. MRI reconstruction results (PSNR/SSIM) of Image 'M11'. (a) the initial image; the reconstructed image by: (b) TV [6]; (c) L1-0.5L2 [40]; (d) BM3D [41]; (e) PANO [42]; (f) DDTF [15]; (g) IRCNN [19]; (h) Ours.

4.5. Analysis of Variance

In general, there are many methods that can be used to test the differences between the two methods. In this paper, we apply the analysis of variance to illustrate the superiority of our method. We compare our approach with the MWCNN and the IRCNN, respectively. We use five different random initial values generated by the Matlab function to test MRI and PET reconstruction tasks. Each task uses the first 15 images in the test set. Fig. 7 (a) and (b) show the distribution of the reconstruction results of the three methods, which illustrate that three methods have significant differences. Fig. 7 (c) and (d) show the difference of the reconstruction results. In MRI reconstruction, at the significance level of 2%, the difference between IRCNN and Ours is significant. In PET reconstruction, at the

significance level of 1%, the difference between IRCNN and Ours is significant; at the significance level of 5%, the difference between MWCNN and Ours is significant. It can be seen from Fig. 7 (a) and (b) that the initial value has a certain influence on the final result of the experiment. Using Matlab command to generate 5 random initial values, the average value of the 5 MRI results of each image is between [28.45, 30.18], and the average value is 29.35. The average value of the 5 PET results of each image is between [32.28, 33.13], and the average value is 32.61. Compared with other methods, our method has a higher average value.

(a) IFFT   (b) TV   (c) L1-0.5L2   (d) PANO

(a) 21.84/0.4710   (b) 23.09/0.5349   (c) 27.12/0.6336   (d) 26.85/0.7469

(e) DDTF   (f) IRCNN   (g) MWCNN   (h) Ours

(e) 27.22/0.8323   (f) 28.25/0.8261   (g) 28.38/0.8246   (h) 28.95/0.8462
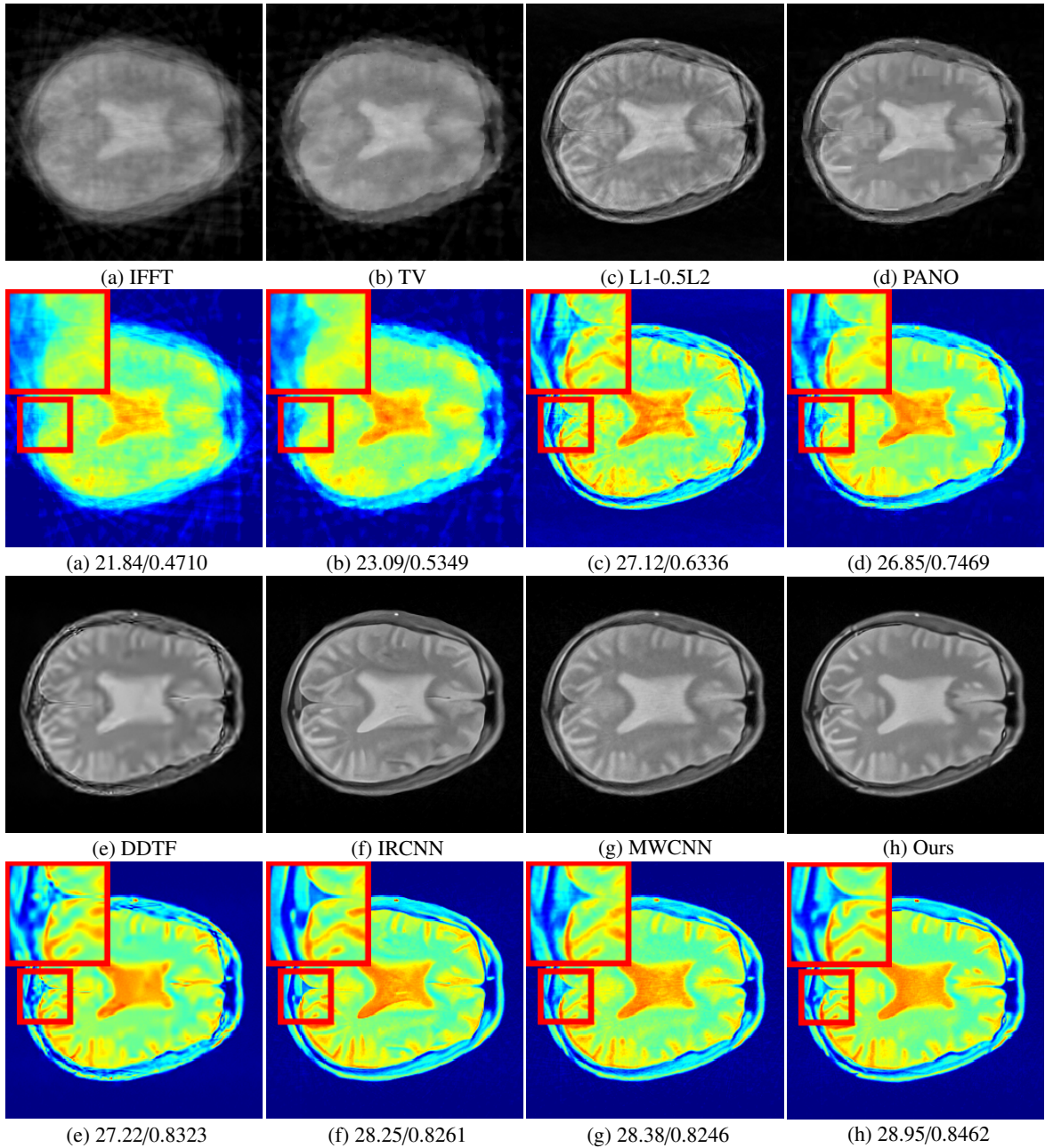
Figure 12. MRI reconstruction results (PSNR/SSIM) of Image 'M29'. (a) the initial image; the reconstructed image by: (b) TV [6]; (c) L1-0.5L2 [40]; (d) PANO [42]; (e) DDTF [15]; (f) IRCNN [19]; (g) MWCNN [24] (h) Ours.

(a) Original   (b) Zoom original   (c) EM

(a) Original   (b) Zoom original   (c) 28.00/0.8251

(d) TV   (e) DDTF   (f) IRCNN   (g) Ours

(d) 31.41/0.9207   (e) 32.71/0.9272   (f) 32.65/0.9183   (g) 33.09/0.9289
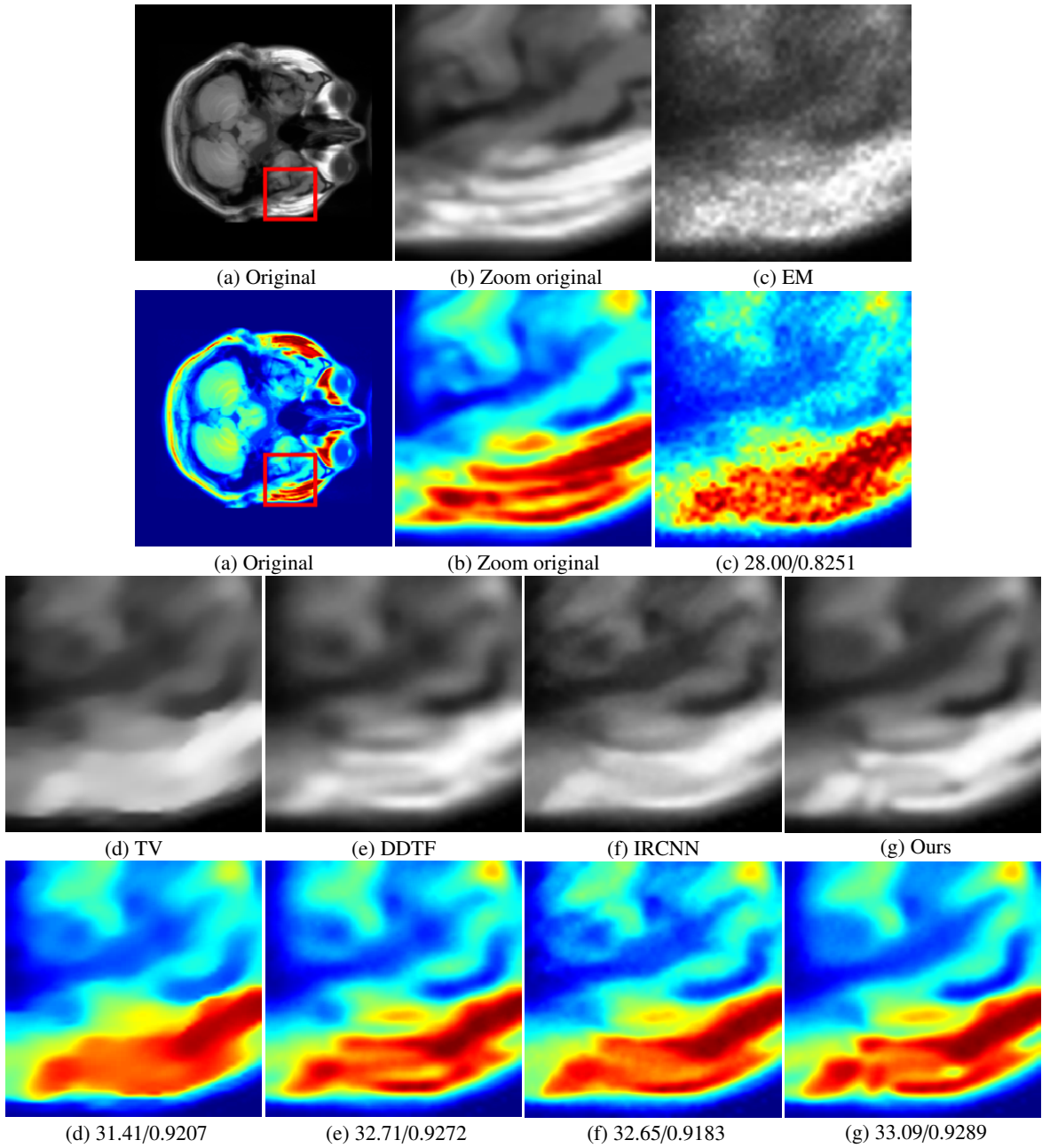
Figure 13. PET reconstruction results (PSNR/SSIM) of image 'P04'. (a) the original image; (b) the zoom part of the original image; (c) the initial image; the reconstructed image by: (d) TV [6]; (e) DDTF [15]; (f) IRCNN [19]; (g) Ours.

4.6. The Results of MRI Reconstruction

To generate MRI data, we use 2-d fast Fourier transform to transfer images into k-space, and sample along 15 radial lines. In order to simulate real data, we add the Gaussian noise with a standard deviation of 0.05 to the sampled data.

To better present the effectiveness of the proposed method, we display the reconstruction results of MRI in Fig. 8, Fig. 11 and Fig. 12. From the visual quality of the reconstructed MRI images, i.e. Figs. 8-12, we find that the TV method [6] generates the staircase effect in (b). For the results generated by the L1-0.5L2 method [40], both staircase and artificial effects can be observed in (c). There are some artifacts shown in the results reconstructed by the BM3D

[41] in (d) and the PANO [42] in (e). For the result reconstructed by the DDTF method [15], the over-smooth effects still exist in (f). From (g), we can see that the noise remains in the results of IRCNN [19]. It is clear that our method can achieve better results both in remaining detailed texture and smoothing. For a more comprehensive analysis of our method, we also display the numerical results of these two different reconstruction problems in Table. 1 with PSNR (dB), SSIM, NMSE, and SAM values. Here, we highlight the best results and underline the second-best results. From Table. 1, we know that our method can generate better results almost at all times. We also plot the barplot with the average results of different methods in Fig. 10, where our method has the highest results in both PSNR and SSIM values of MRI reconstruction results, obviously. From the average results, we know that our method is superior to stand-alone deep learning methods in two changeable tasks. In average PSNR value, our new proposed method is superior more than 1 dB over the IRCNN [19] and more than 2 dB over the tight frame-based method DDTF [15] in MRI reconstruction.

Relatively speaking, our method can handle complex problems well. For example, the results of PET experiments show that our scheme is much better than IRCNN. For simple tasks, our method has certain effects. For example, the results of MRI experiments show that our approach is better than MWCNN. The model we propose is a general framework. If there are better regular terms (such as denoiser), there will be better results. The ideas in this article can be widely used in medical image processing.

4.7. The Results of PET Reconstruction

For the PET reconstruction problem, we compare five methods. The visual quality is displayed in Fig. 13, Fig. 14, and Fig. 15, which demonstrates our method has the best performance in PET reconstruction among these compared methods. Due to the high density of our degradation, the classical EM algorithm does not remove the noise cropped in the images well. With no expectation, the staircase effects also occur in (d). The DDTF method generates a good result, but there are some artifacts in (e) (see the rectangle part). The result generated by IRCNN is some noise remains. While our method overcomes the artifacts and noise at the same time, generates a better reconstruction result significantly. The PSNR (dB) and SSIM values are in Table. 2. We highlight the highest PSNR and SSIM values and underline the second-best results. From the highlighted results, we know that the proposed model can better handle the PET reconstruction task than other methods. The barplot with the average results of different methods in Fig. 10 also demonstrates the superiority of our model. In PET reconstruction, our method is superiority 0.6 dB than IRCNN [19] and 0.66 dB than DDFT [15] in PSNR. The deep learning-based methods are essential, which provide a series of solutions for vision tasks. However, the interpretation of the deep learning-based methods is still an open question. As we know, medical image reconstruction requires exact results to diagnose the patient's condition. Meanwhile, deep learning-based methods have shown great success in image processing tasks. However, the network is a black box and the inside works are unknown. Therefore, we consider plugging the deep learning-based method to solve a sub-problem of medical image reconstruction. From the results of the proposed hybrid model, the constructed result is better than the traditional reconstruction methods. In addition, the doubt of the deep learning-based models was also mitigated. Hence, the proposed model improved the interpretability of the deep learning-based models.

4.8. The Reconstruction with Rician Noise

The raw data collected by the magnetic resonance apparatus is K-space data, which contains two parts of the signal, i.e., the real part and the imaginary part. The real and imaginary parts have additive white Gaussian noise with zero mean, respectively. Generally, Fourier transform is performed on K-space data to obtain image domain data. The Fourier transform does not change the form of noise, hence the image domain data we get is a complex signal u_c whose expression is

$$u_c = (u_r + n_r) + (u_i + n_i)i, \tag{25}$$

where u_r and u_i are the real and imaginary parts of u_c, respectively, n_r and n_i are the Gaussian noise. In fact, the image we observed is the amplitude image obtained by modulo operation, that is

$$u = |u_c| = \sqrt{(u_r + n_r)^2 + (u_i + n_i)^2}. \tag{26}$$

Obviously, the final obtained image u is no longer a simple additive Gaussian noise, but a Rician noise related to the signal.

Therefore, it is significant to perform the Rician noise reconstruction task. In this paper, we consider the MRI and PET reconstruction with non-Gaussian noise. Here we conduct a simple image reconstruction experiment with Rician noise. Mathematically, the difference between additive Gaussian noise and Rician noise primarily lies in the data fitting term of the model. Specifically, we adjust the data fitting term to follow the Rician distribution while maintaining the denoiser subproblem unchanged. As a result, the MWCNN does not need to be retrained and can continue to serve as a denoiser. The Rician noise level is set to be 0.08 and the reconstruction result is presented in Fig. 9. It can be seen that we have a better reconstruction effect than MWCNN, which reflects the validity of our strategy.
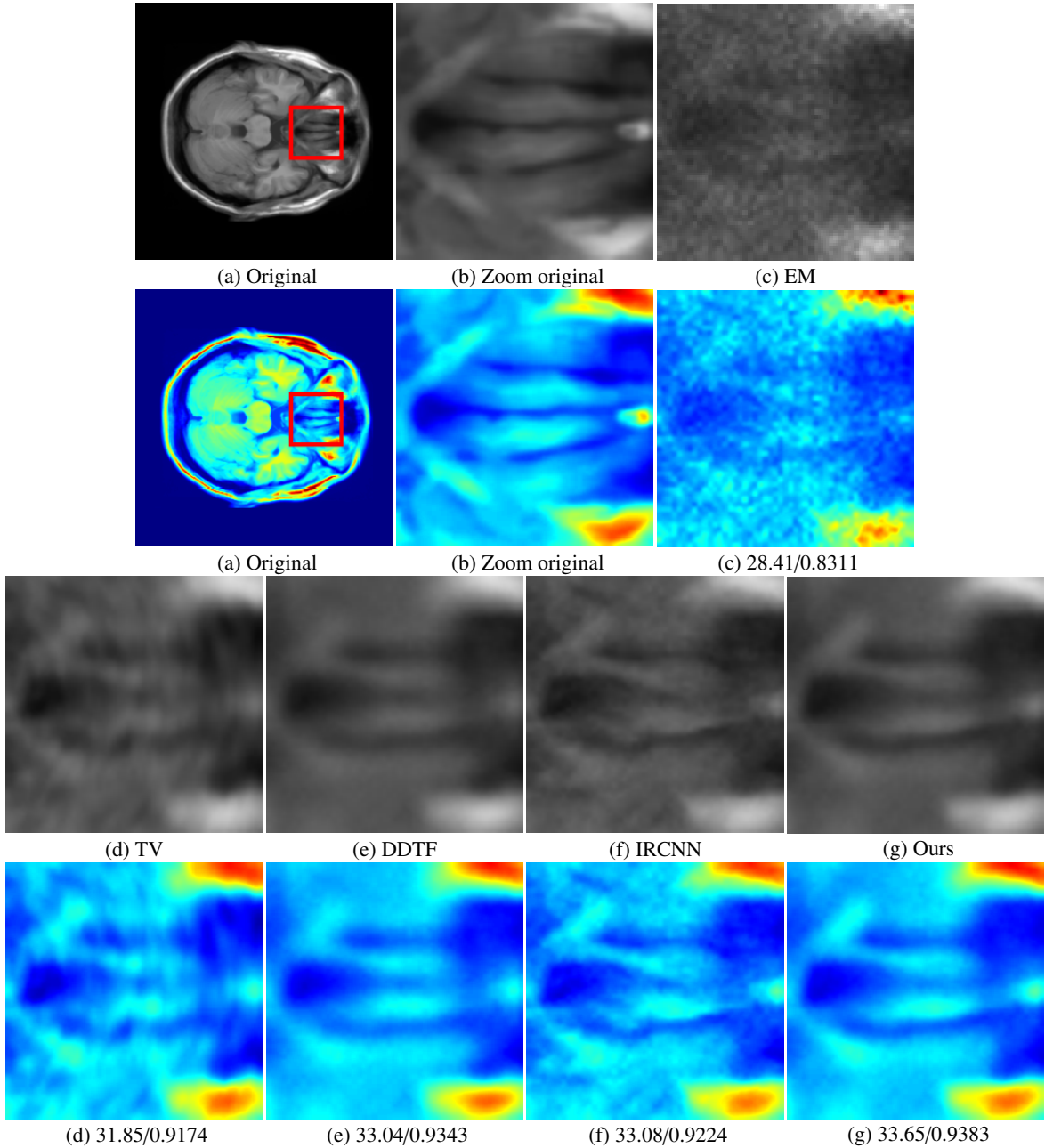
Figure 14. PET reconstruction results (PSNR/SSIM) of image 'P06'. (a) the original image; (b) the zoom part of the original image; (c) the initial image; the reconstructed image by: (d) TV [6]; (e) DDTF [15]; (f) IRCNN [19]; (g) Ours.

(a) Real image   (b) EM   (c) TV

(a) Real image   (b) 36.42/0.9611   (c) 35.12/0.9402

(d) DDTF   (e) IRCNN   (f) MWCNN   (g) Ours

(d) 40.17/0.9752   (e) 39.10/0.9671   (f) 40.02/0.9757   (g) 40.52/0.9789
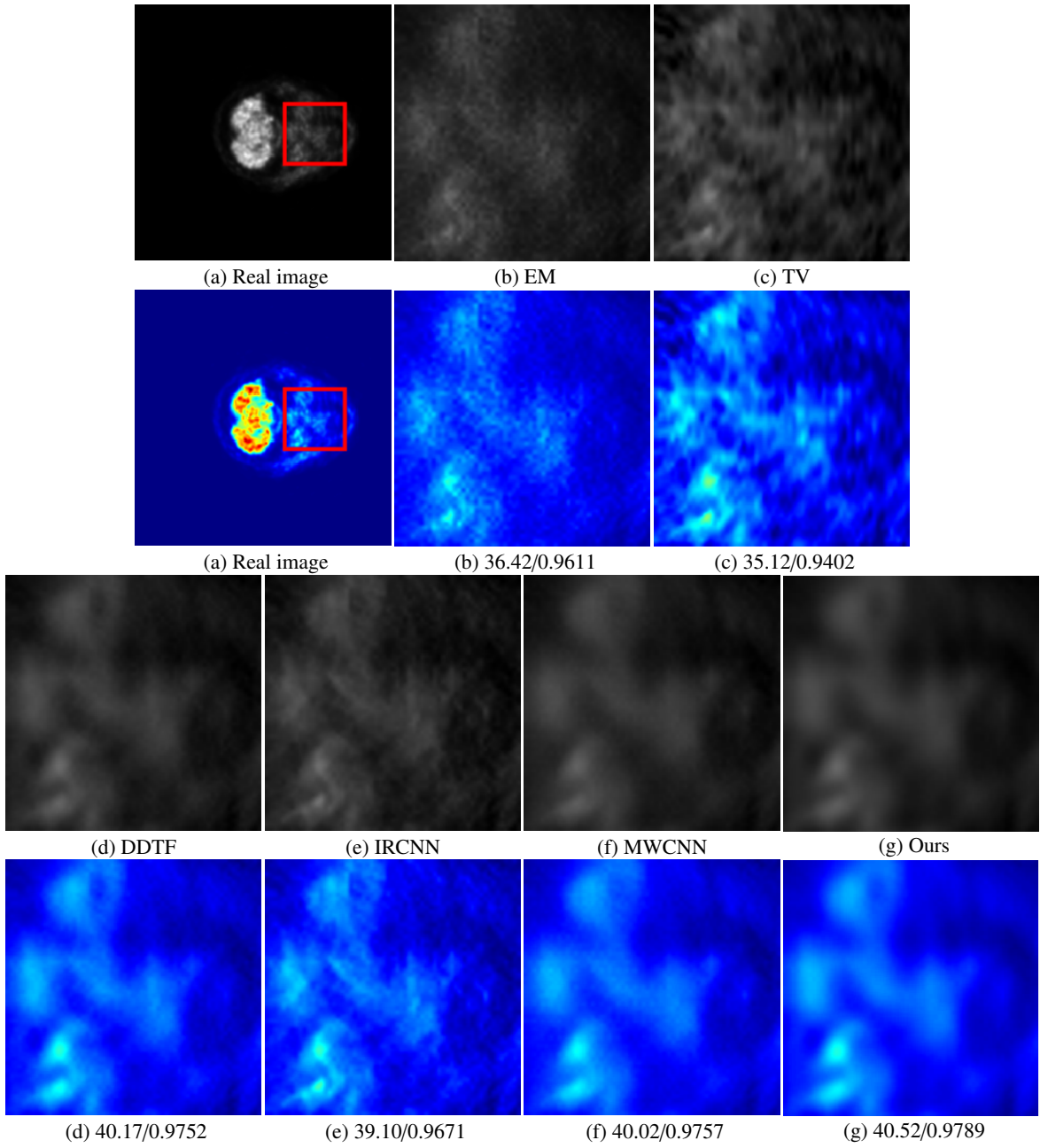
Figure 15. PET reconstruction results (PSNR/SSIM) of image 'P18'. (a) the real image; (b) the initial image; the reconstructed image by: (c) TV [6]; (d) DDTF [15]; (e) IRCNN [19]; (f) MWCNN [24]; (g) Ours.

5. Conclusion

In this paper, we discuss an interpretable image reconstruction framework. Most deep learning-based methods cannot give a good explanation of the results. Therefore, the result of medical image reconstruction directly obtained by deep learning-based methods is doubtful. To solve this problem, we denote the network as a sub-problem. Through the iteration of the proposed algorithm, not only can the traditional method and the network method be well connected, but also the advantages of the network method can be well used. The model we proposed is a hybrid model which is difficult to solve, we introduced the PAM algorithm to solve this model, and we analyzed the convergence of

our method through numerical results. Furthermore, multiple training methods allow us to choose the corresponding parameters automatically. The different medical image reconstruction tasks are applied to demonstrate the effectiveness of our method. The proposed model has superiority over several state-of-the-art methods in both MRI and PET reconstruction tasks.

6. Acknowledgment

References

[1] J.-F. Cai, J. K. Choi, K. Wei, Data driven tight frame for compressed sensing MRI reconstruction via off-the-grid regularization, SIAM Journal on Imaging Sciences 13 (3) (2020) 1272–1301.
[2] C. Huang, T. Wu, J. Li, B. Dong, T. Zeng, Single-particle reconstruction in cryo-EM based on three-dimensional weighted nuclear norm minimization, Pattern Recognition 143 (2023) 109736.
[3] T. Wu, M. K. Ng, X.-L. Zhao, Sparsity reconstruction using nonconvex TGpV-shearlet regularization and constrained projection, Applied Mathematics and Computation 410 (2021) 126170.
[4] B. Shi, F. Gu, Z.-F. Pang, Y. Zeng, Remove the salt and pepper noise based on the high order total variation and the nuclear norm regularization, Applied Mathematics and Computation 421 (2022) 126925.
[5] G. Chen, B. Dong, Y. Zhang, W. Lin, D. Shen, P.-T. Yap, XQ-SR: joint XQ space super-resolution with application to infant diffusion MRI, Medical image analysis 57 (2019) 44–55.
[6] M. J. Ehrhardt, K. Thielemans, L. Pizarro, D. Atkinson, S. Ourselin, B. Hutton, S. Arridge, Joint reconstruction of PET-MRI by exploiting structural similarity, Inverse Problems 31 (2015) 1–23.
[7] T. Wu, C. Huang, Z. Jin, Z. Jia, M. K. Ng, Total variation based pure quaternion dictionary learning method for color image denoising., International Journal of Numerical Analysis & Modeling 19 (5).
[8] Y.-W. Wen, M. Zhao, M. Ng, Cartoon and texture decomposition for color image in opponent color space, Applied Mathematics and Computation 414 (2022) 126654.
[9] T. Wu, C. Huang, X. Gu, J. Niu, T. Zeng, Finding robust minimizer for non-convex phase retrieval, Inverse Problems and Imaging 18 (1) (2024) 286–310.
[10] L. I. Rudin, S. Osher, E. Fatemi, Nonlinear total variation based noise removal algorithms, Physica D 60 (1992) 258–268.
[11] L. Guo, X.-L. Zhao, X.-M. Gu, Y.-L. Zhao, Y.-B. Zheng, T.-Z. Huang, Three-dimensional fractional total variation regularized tensor optimized model for image deblurring, Applied Mathematics and Computation 404 (2021) 126224.
[12] C. Wang, M. Tao, J. G. Nagy, Y. Lou, Limited-angle CT reconstruction via the L_1/L_2 minimization, SIAM Journal on Imaging Sciences 14 (2) (2021) 749–777.
[13] M. Unser, Texture classification and segmentation using wavelet frames, IEEE Transactions on Image Processing : A Publication of the IEEE Signal Processing Society 4 (11) (1995) 1549–1560.
[14] X. Jia, B. Dong, Y. Lou, S. B. Jiang, GPU-based iterative cone-beam CT reconstruction using tight frame regularization, Physics in Medicine & Biology 56 (13) (2011) 3787.
[15] J. Choi, C. Bao, X. Zhang, PET-MRI joint reconstruction by joint sparsity based tight frame regularization, SIAM Journal on Imaging Science 11 (2018) 1179–1204.
[16] W. Zhou, J. Cai, H. Gao, Adaptive tight frame based medical image reconstruction: a proof-of-concept study for computed tomography, Inverse Problems 29 (2013) 125–146.
[17] R. Zhan, B. Dong, CT image reconstruction by spatial-radon domain data-driven tight frame regularization, SIAM Journal of Imaging Science 9 (2016) 1063–1083.
[18] L. A. Shepp, Y. Vardi, Maximum likelihood reconstruction for emission tomography, IEEE Transactions on Medical Imaging (1982) 113–122.
[19] K. Zhang, W. Zuo, S. Gu, L. Zhang, Learning deep CNN denoiser prior for image restoration, 2017 IEEE Conference on Computer Vision and Pattern Recognition (CVPR) (2017) 2808–2817.
[20] K. Mei, A. Jiang, J. Li, J. Ye, M. Wang, An effective single-image super-resolution model using squeeze-and-excitation networks, in: ICONIP, 2018, pp. 542–553.
[21] G. Gao, Z. Xu, J. Li, J. Yang, T. Zeng, G. Qi, CTCNet: A cnn-transformer cooperation network for face image super-resolution. arxiv 2022, IEEE Transactions on Image Processing 32 (2023) 1978 – 1991.
[22] B. Cheng, J. Li, Y. Chen, T. Zeng, Snow mask guided adaptive residual network for image snow removal, Computer Vision and Image Understanding 236 (2023) 103819.
[23] J. Li, H. Yang, Q. Yi, F. Fang, G. Gao, T. Zeng, G. Zhang, Multiple degradation and reconstruction network for single image denoising via knowledge distillation, in: Proceedings of the IEEE/CVF Conference on Computer Vision and Pattern Recognition, 2022, pp. 558–567.
[24] P. Liu, H. Zhang, K. Zhang, L. Lin, W. Zuo, Multi-level wavelet-CNN for image restoration, in: Proceedings of the IEEE Conference on Computer Vision and Pattern Recognition Workshops, 2018, pp. 773–782.

[25] T. Wu, W. Li, S. Jia, Y. Dong, T. Zeng, Deep multi-level wavelet-CNN denoiser prior for restoring blurred image with Cauchy noise, IEEE Signal Processing Letters 27 (2020) 1635–1639.

[26] B. Dong, A note on machine learning approach for computational imaging, arXiv preprint arXiv:2202.11883 (2022) 1-17.

[27] Z. Wu, C. Huang, T. Zeng, Extrapolated plug-and-play three-operator splitting methods for nonconvex optimization with applications to image restoration, arXiv preprint arXiv:2403.01144.

[28] B. Dong, J. Li, Z. Shen, X-ray CT image reconstruction via wavelet frame based regularization and radon domain inpainting, Journal of Scientific Computing 54 (2013) 333–349.

[29] B. Dong, Z. Shen, P. Xie, Image restoration: A general wavelet frame based model and its asymptotic analysis, SIAM Journal on Mathematical Analysis 49 (1) (2017) 421–445.

[30] B. Dong, Sparse representation on graphs by tight wavelet frames and applications, Applied and Computational Harmonic Analysis 42 (3) (2017) 452–479.

[31] S. Baoshun, Q. Lian, H. Chang, Deep prior-based sparse representation model for diffraction imaging: A plug-and-play method, Signal Processing 168 (2019) 1–15.

[32] F. Jia, X. Tai, Regularized U-net for automated pancreas segmentation, Proceedings of the Third International Symposium on Image Computing and Digital Medicine (2019) 113–117.

[33] M. Ding, T.-Z. Huang, T.-H. Ma, X.-L. Zhao, J.-H. Yang, Cauchy noise removal using group-based low-rank prior, Applied Mathematics and Computation 372 (2020) 124971.

[34] C. Huang, M. K. Ng, T. Wu, T. Zeng, Quaternion-based dictionary learning and saturation-value total variation regularization for color image restoration, IEEE Transactions on Multimedia (2021) 1–13.

[35] S. Pyatykh, J. Hesser, L. Zheng, Image noise level estimation by principal component analysis, IEEE Transactions on Image Processing 22 (2) (2013) 687–699.

[36] H. Attouch, J. Bolte, P. Redont, A. Soubeyran, Proximal alternating minimization and projection methods for nonconvex problems: An approach based on the kurdyka-Łojasiewicz inequality, Mathematics of Operations Research 35 (2) (2010) 438–457.

[37] J. Wang, J. Cai, Data-driven tight frame for multi-channel images and its application to joint color-depth image reconstruction, Journal of the Operations Research Society of China 3 (2015) 99–115.

[38] L. Chen, X. Li, D. Sun, K.-C. Toh, On the equivalence of inexact proximal ALM and ADMM for a class of convex composite programming, Mathematical Programming (2019) 1–51.

[39] W. Jin, Y. Censor, M. Jiang, Bounded perturbation resilience of projected scaled gradient methods, Computational Optimization and Applications 63 (2016) 365–392.

[40] Y. Lou, T. Zeng, S. Osher, J. Xin, A weighted difference of anisotropic and isotropic total variation model for image processing, SIAM Journal on Imaging Science 8 (3) (2015) 1798–1823.

[41] E. Eksioglu, Decoupled algorithm for MRI reconstruction using nonlocal block matching model: BM3D-MRI, Journal of Mathematical Imaging and Vision 56 (3) (2016) 430–440.

[42] X. Qu, Y. Hou, F. Lam, D. Guo, J. Zhong, Z. Chen, Magnetic resonance image reconstruction from undersampled measurements using a patch-based nonlocal operator, Medical Image Analysis 18 (6) (2014) 843–856.

[43] D. Martin, C. Fowlkes, D. Tal, J. Malik, A database of human segmented natural images and its application to evaluating segmentation algorithms and measuring ecological statistics, in: Proceedings Eighth IEEE International Conference on Computer Vision. ICCV 2001, Vol. 2, 2001, pp. 416–423.

[44] A. Ignatov, R. Timofte, et al., Pirm challenge on perceptual image enhancement on smartphones: report, in: European Conference on Computer Vision (ECCV) Workshops, 2019.

[45] K. Ma, Z. Duanmu, Q. Wu, Z. Wang, H. Yong, H. Li, L. Zhang, Waterloo Exploration Database: New challenges for image quality assessment models, IEEE Transactions on Image Processing 26 (2) (2017) 1004–1016.

[46] J. Deng, W. Dong, R. Socher, L. J. Li, K. Li, L. Fei-Fei, Imagenet: A large- scale hierarchical image database, IEEE Conference on Computer Vision and Pattern Recognition(CVPR) (2009) 248–255.

[47] C. A. Cocosco, V. Kollokian, R. K.-S. Kwan, G. B. Pike, A. C. Evans, Brainweb: Online interface to a 3D MRI simulated brain database, in: NeuroImage, Citeseer, 1997.

[48] A. Suinesiaputra, B. R. Cowan, J. P. Finn, C. G. Fonseca, A. H. Kadish, D. C. Lee, P. Medrano-Gracia, S. K. Warfield, W. Tao, A. A. Young, Left ventricular segmentation challenge from cardiac MRI: a collation study, in: International Workshop on Statistical Atlases and Computational Models of the Heart, Springer, 2011, pp. 88–97.

[49] R. Wang, S. Cao, K. Ma, Y. Zheng, D. Meng, Pairwise learning for medical image segmentation, Medical Image Analysis 67 (2021) 101876.

[50] Z. Wang, A. C. Bovik, H. R. Sheikh, E. P. Simoncelli, Image quality assessment: from error visibility to structural similarity, IEEE Transactions on Image Processing 13 (4) (2004) 600–612.

[51] A. M. Eskicioglu, P. S. Fisher, Image quality measures and their performance, IEEE Transactions on Communications 43 (12) (1995) 2959–2965.

[52] F. A. Kruse, A. Lefkoff, J. Boardman, K. Heidebrecht, A. Shapiro, P. Barloon, A. Goetz, The spectral image processing system (SIPS)—interactive visualization and analysis of imaging spectrometer data, Remote Sensing of Environment 44 (2-3) (1993) 145–163.

[53] F. Knoll, J. Zbontar, A. Sriram, M. J. Muckley, M. Bruno, A. Defazio, M. Parente, K. J. Geras, J. Katsnelson, H. Chandarana, et al., fastMRI: A publicly available raw k-space and DICOM dataset of knee images for accelerated MR image reconstruction using machine learning, Radiology: Artificial Intelligence 2 (1) (2020) e190007.

[54] W. Zhou, S. Yang, C. Zhang, S. Fu, Adaptive tight frame based multiplicative noise removal, SpringerPlus 5 (1) (2016) 1–12.

[55] E. Ryu, J. Liu, S. Wang, X. Chen, Z. Wang, W. Yin, Plug-and-play methods provably converge with properly trained denoisers, Proceedings of the International Conference on Machine Learning (2019) 5546–5557.